

LES of a pressurized sooting aero-engine model burner using a computationally efficient discrete sectional method coupled to tabulated chemistry

J.M. García-Oliver^a, J.M. Pastor^{a,*}, I. Olmeda^a, A. Kalbhor^c, D. Mira^b, J.A. van Oijen^c

^a CMT-Clean Mobility & Thermo fluids, Universitat Politècnica de València, Spain

^b Barcelona Supercomputing Center (BSC), Spain

^c Department of Mechanical Engineering, Eindhoven University of Technology, Netherlands

ARTICLE INFO

Keywords:

Soot, Large-eddy simulation
Discrete sectional method
Particle size distribution
Flamelet generated manifold
Gas turbine combustor

ABSTRACT

This work is focused on the modeling and analysis of soot formation and oxidation in the pressurized ethylene-based model burner investigated at DLR. This burner features a dual swirler configuration for the primary air supply and includes secondary dilution jets inside the combustion chamber, showing reacting flow characteristics representative of the RQL combustor technology. Large-eddy simulations (LES) of the DLR burner are conducted here to assess a coupling approach between flamelet generated manifold (FGM) chemistry and discrete sectional method (DSM) based soot model with clustering method. First, a validation of the numerical results is conducted for the gas velocity and temperature fields, and good agreement is obtained for both mean and fluctuating quantities. The Soot Volume Fraction (SVF) computed from LES shows a satisfactory agreement with the experimental data in both SVF distribution and magnitude. The analysis also includes a numerical investigation of the soot production and the Particle Size Distributions (PSD). Finally, the configuration without secondary air is evaluated and an accurate prediction of the SVF field is also obtained. In this case, the absence of dilution air strongly influences the central region of the combustion chamber, and soot distribution and PSD are mainly affected by transport and dilution, not oxidation. It is finally concluded the proposed modeling framework is capable of predicting the soot field and particle size distributions inside the combustor for both operating conditions.

Novelty and significance

This work presents a large-eddy simulation (LES) study of soot production and particle size distribution (PSD) using a recently developed coupling between a Flamelet Generated Manifold combustion description and a Discrete Sectional Method soot model. This model features clustered sections with tabulated source terms to get a computationally efficient LES. Good qualitative and quantitative predictions of the soot volume fraction field have been obtained in the DRL-RQL model combustor, which is a target case from the International Sooting Flame workshop. Computational results show that soot particles persist in the periphery of the combustion chamber, downstream of the formation region, where other state-of-the-art simulations overestimate oxidation rate. In addition, the sectional model provided the PSD temporal and spatial variations related to soot formations and oxidation processes. Finally, the effect of excluding the secondary oxidation is also well captured in the simulations, where soot appears in the inner recirculation zone of the burner.

1. Introduction

Mitigation of combustion-generated pollutant emissions is nowadays an important challenge in the development of next-generation gas turbine burners. In particular, a thorough understanding of the particulate matter formation processes in such applications is crucial, due to their harmful effects on health and the environment. Since manufacturing and testing realistic burners in different operating conditions is very expensive, Computational Fluid Dynamics (CFD) methods are an excellent alternative to study combustion processes in such practical applications, due to the reduction in the cost of analysis, combined with detailed descriptions of the physical phenomena and overall system performance [1]. For instance, Large-Eddy Simulations (LES) have proven to be a powerful tool for accurately modeling turbulent reactive flows in complex geometries with an affordable computational cost [2, 3]. However, numerical prediction of soot formation and oxidation in

* Corresponding author.

E-mail address: jopasen@mot.upv.es (J.M. Pastor).

<https://doi.org/10.1016/j.combustflame.2023.113198>

Received 27 July 2023; Received in revised form 9 November 2023; Accepted 13 November 2023

Available online 30 November 2023

0010-2180/© 2023 The Author(s). Published by Elsevier Inc. on behalf of The Combustion Institute. This is an open access article under the CC BY-NC-ND license (<http://creativecommons.org/licenses/by-nc-nd/4.0/>).

combustion chambers remains a great challenge due to strong coupling between the turbulent flow, gas-phase chemistry, and soot particle processes [4].

Comprehensive soot modeling requires addressing key processes related to soot kinetics and aerosol dynamics [4,5], such as nucleation from gas-phase precursors, surface reactions, or particle-to-particle interactions. Although different pathways have been proposed, it is widely assumed that polycyclic aromatic hydrocarbons (PAHs) play a major role in the soot nucleation step [6]. Accurate prediction of PAH precursor and other species involved in soot growth and oxidation demands detailed chemistry, involving large fuel oxidation kinetic mechanisms. The direct application of detailed kinetics in large-scale simulations is unaffordable, and different strategies have been proposed for reducing the computational cost [7]. In this regard, tabulated chemistry methods, such as FGM [8] or FPV [9], have been applied to integrate detailed kinetic mechanisms with PAH-based soot models in LES of flames and combustors [10,11]. Alternatively, reduced kinetic schemes have been used in finite-rate chemistry LES coupled to semi-empirical acetylene-based soot models [12], but also to more complex lumped PAH chemistry [13–15] at the expense of higher computational effort.

The soot aerosol dynamics are described by the population balance equation (PBE) of the particle Number Density Function (NDF). Solving the PBE is not feasible in turbulent flows, and the method of moments (MoM) [16] and the discrete sectional method (DSM) [17] have been proposed to model the NDF. The particle distribution is approximated in MoM by solving transport equations for the low-order moments, while the continuous distribution is discretized by a finite amount of sections for the DSM. The latter method is able to predict different distribution shapes but becomes computationally demanding when the number of sections is increased to improve accuracy. Additional transport equations for soot sections, at least over 30, and the computation of the source terms related to soot kinetics and particle dynamics limit its application to complex configurations. Further research is then required to develop predictive methods for soot formation at affordable computational requirements for practical applications.

To reduce the CPU cost, Franzelli et al. [18] developed a three-equation model based on mono-disperse closure of the source terms from a DSM. This approach was able to fairly predict soot volume fraction in laminar and turbulent flames, but does not explicitly provide information about the particle distribution, and its reconstruction method requires further validation. An efficient coupling between a DSM soot model and FGM tabulated chemistry was recently proposed by Kalbhor et al. [19,20]. This strategy is based on the clustering of soot sections (CDSM) and the tabulation of pre-computed soot source terms, which retains the information on the size distribution of soot particles at reduced computational cost. This approach has shown good predictive capabilities in laminar flames [19] and high-pressure igniting sprays [21], but needs to be further tested in realistic conditions. The present study aims to assess the FGM-CDSM framework for LES of gas-turbine combustors, where the trade-off between CPU cost and accuracy is a major concern.

In this context, the aero-engine model combustor developed at the German Aerospace Center (DLR) by Geigle et al. [22,23] has been widely studied in terms of turbulent combustion and soot formation characteristics and it is part of the ISF Workshop [24] for turbulent flames. This configuration has been selected to evaluate the LES-FGM-CDSM approach. It is a pressurized burner featuring a dual swirler configuration for the primary air supply, and generating a strong recirculation region inside the combustion chamber. Secondary air is injected downstream, creating a soot oxidation zone typical of the Rich-Burn/Quick-Mix/Lean-Burn (RQL) combustor concept. Different modeling strategies have been used over the last few years to predict soot emissions in this burner [24]. In Refs. [12,13,25], semi-empirical two-equation soot models and reduced kinetic mechanisms coupled to different turbulent combustion approaches were employed to predict

soot quantity. In general, the numerical results were able to qualitatively capture soot distribution, although important discrepancies were observed in the soot volume fraction magnitude depending on the combustion modeling and chemistry description. In addition, these modeling approaches do not account for particle characteristics and size distributions. Simulations with detailed soot chemistry and particle dynamics of this burner were conducted in [26], where the hybrid MoM [27] was coupled to tabulated chemistry. A good qualitative agreement with the experimental data was obtained, but the SVF was strongly overpredicted. A similar soot description was used in [28] showing a fair prediction of the soot field for the reference operating condition of the DLR combustor. Conversely, the soot distribution was not captured for the burner configuration without secondary air injection. In [29] the burner simulation with Split-based Extended Quadrature MoM [30] was able to capture soot field distribution but the magnitude was underestimated by a factor of three. Recently, DSM has been applied to simulate this burner coupled to tabulated [31] and to finite-rate [32] chemistry. Good qualitative and quantitative soot predictions were obtained, though soot oxidation in the outer part of the burner is overestimated, such as in most of the simulations previously discussed. Particle Size Distribution (PSD) information was only provided by [31]. Unfortunately, validation was not possible due to the lack of experimental measurements.

The objectives of this work are twofold (i) to evaluate predictive capabilities of the LES-FGM-CDSM modeling framework for soot concentration and particle size distribution, and (ii) to analyze the soot formation and oxidation processes within the DLR pressurized burner under different flow conditions, including cases with and without secondary air injection. The paper is structured as follows: first, the modeling approach for turbulent combustion and soot prediction is described. Subsequently, the experimental test case and numerical setup are presented in Section 3. Finally, the results obtained are discussed in Section 4, followed by the main conclusions of this work in Section 5.

2. Modeling approach

2.1. Turbulent combustion model

2.1.1. Flamelet method

The thermo-chemical state of the flame in this configuration is described by the flamelet method [33]. A scale separation between the flow and the chemistry is assumed, so that the flame structure can be defined by a composition of one-dimensional (1D) flames. In order to account for strain effects on the thermodynamic behavior of the reacting layer, laminar diffusion flamelets at different strain rates are tabulated until the extinction point is encountered. An extinguishing flamelet initiated from the last stable instance (extinction point) is used as a natural continuation of this two-dimensional manifold [34], conducting an unsteady calculation to account for the transient development to the mixing state.

The combustion process in this configuration occurs in partially premixed conditions due to the rapid fuel/air mixing. Despite fuel and air being injected separately, partial premixing is achieved before the mixture interacts with the reacting layer, and then the flame burns across a wide range of equivalence ratios, even outside the flammability range. Due to such conditions, the tabulation of counterflow diffusion flamelets is employed here. The flamelet equations are solved in physical space with the chem1D code [35] using a unity Lewis number approach. The chemistry for ethylene fuel is taken from a 214-species and 1537 reactions kerosene surrogates mechanism [36] including recent developments for PAH soot precursors [37].

2.1.2. Control variables

Three controlling variables are used to characterize the thermochemical state of the flamelets composing the manifold: mixture fraction Z , progress variable Y_c , and scaled enthalpy \mathcal{H} . The mixture fraction is determined by Bilger's formula, while the progress variable Y_c in our study is defined as:

$$Y_c = \sum_{k=1}^N \frac{a_k}{W_k} Y_k, \quad (1)$$

with $N = 6$ using $Y_k = \{Y_{CO_2}, Y_{CO}, Y_{H_2}, Y_{H_2O}, Y_{C_2H_2}, Y_{A4}\}$, and W_k being the molar weight of the chemical species. The contribution of each species to the progress variable Y_k is given by the coefficients $a_k = \{4.0, 1.0, 1.0, 2.0, -1.0, 2000\}$ respectively. The current progress variable is defined to facilitate unique mapping of thermochemical variables in the composition space for both combustion chemistry and soot-gas phase chemistry interaction. While the progress variable definition generally includes main combustion products, those species do not have sensitivity to recover slow developing processes like PAH formation or soot. Therefore, additional key species involved in soot inception and growth, such as A4 and C_2H_2 , have been incorporated in the progress variable definition to account for the evolution of soot in the manifold space [19]. Note that A4 is a PAH soot precursor with slow formation chemistry that is restricted to low strain rates, and its contribution to the progress variable is selected to improve the sensitivity in the FGM [38]. Nevertheless, since the A4 species is not explicitly transported for the calculation of soot source terms, the accuracy of the current FGM-CDSM framework is not significantly impacted by adding A4 in the progress variable definition. To facilitate the flamelet manifold tabulation (access and retrieval), a scaled progress variable C is then defined as:

$$C = \frac{Y_c - Y_{c,min}}{Y_{c,max} - Y_{c,min}}. \quad (2)$$

The effects of heat loss on the flamelet database are considered by the tabulation of strained diffusion flames at different enthalpy levels. For given boundary temperature of reactant and oxidizer streams, the local enthalpy deficit is generated through a radiative source term in the energy equation (f_{rad}). Different enthalpy levels are reached by varying the radiative term, which can be tabulated in terms of the scaled enthalpy \mathcal{H} as defined in Eq. (3).

$$\mathcal{H} = \frac{h - h_{min}}{h_{max} - h_{min}}. \quad (3)$$

For a particular value of the total enthalpy h , the scaled enthalpy \mathcal{H} is defined by the maximum and minimum enthalpy levels, h_{max} and h_{min} , given in the low-dimensional manifold space.

2.1.3. Governing equations

The equations describing the reacting flow correspond to the low-Mach number approximation of the Navier–Stokes with the energy equation represented by the total enthalpy (sensible and chemical). A Favre-filtered description of the governing equations is followed to avoid the modeling of terms including density fluctuations. Favre-filtering of any quantity ϕ is denoted by $\bar{\phi}$, while Reynolds-filtering is given by $\tilde{\phi}$. The filtered governing equations for LES correspond to the continuity, momentum and enthalpy. In addition, transport equations for the filtered controlling variables \tilde{Z} and \tilde{Y}_c are defined in order to describe the chemical evolution of the reacting flow. The system of equations reads:

$$\frac{\partial \bar{\rho}}{\partial t} + \nabla \cdot (\bar{\rho} \bar{\mathbf{u}}) = 0, \quad (4)$$

$$\frac{\partial \bar{\rho} \bar{\mathbf{u}}}{\partial t} + \nabla \cdot (\bar{\rho} \bar{\mathbf{u}} \bar{\mathbf{u}}) = -\nabla \cdot \bar{\tau}_M - \nabla \bar{p} + \nabla \cdot (\bar{\mu} \nabla \bar{\mathbf{u}}), \quad (5)$$

$$\frac{\partial \bar{\rho} \bar{h}}{\partial t} + \nabla \cdot (\bar{\rho} \bar{\mathbf{u}} \bar{h}) = -\nabla \cdot \bar{\tau}_h + \nabla \cdot (\bar{\rho} \bar{D} \nabla \bar{h}), \quad (6)$$

$$\frac{\partial \bar{\rho} \tilde{Z}}{\partial t} + \nabla \cdot (\bar{\rho} \tilde{\mathbf{u}} \tilde{Z}) = -\nabla \cdot \bar{\tau}_Z + \nabla \cdot (\bar{\rho} \bar{D} \nabla \tilde{Z}), \quad (7)$$

$$\frac{\partial \bar{\rho} \tilde{Y}_c}{\partial t} + \nabla \cdot (\bar{\rho} \tilde{\mathbf{u}} \tilde{Y}_c) = -\nabla \cdot \bar{\tau}_{Y_c} + \nabla \cdot (\bar{\rho} \bar{D} \nabla \tilde{Y}_c) + \bar{\omega}_{Y_c}, \quad (8)$$

where standard notation is used for all the quantities with $\bar{\rho}$, $\bar{\mathbf{u}}$, \bar{h} , \bar{D} , $\bar{\mu}$, $\bar{\omega}_{Y_c}$ represent the density, velocity vector, total enthalpy, diffusivity, pressure, dynamic viscosity and progress variable source term using filtered quantities. The scaled enthalpy $\tilde{\mathcal{H}}$ is obtained directly from the enthalpy, see Eqs. (3) and (6). The τ term stands for the unresolved or subgrid terms related to the filtering operation and applies to the unresolved fluxes for momentum $\bar{\tau}_M$, enthalpy $\bar{\tau}_h$, mixture fraction $\bar{\tau}_Z$ and progress variable $\bar{\tau}_{Y_c}$; which are closed using a gradient diffusion approach. The subgrid viscous stress tensor is determined based on the Stokes' assumption and the turbulence contribution is obtained by the use of the Boussinesq approximation [39]. A unity-Lewis number assumption has been made to simplify the scalar transport in the governing equations. Heating due to viscous forces is neglected in the enthalpy equation and the unresolved heat flux is modeled using a gradient diffusion approach [40]. The modeling framework is closed by an appropriate expression for the subgrid-scale viscosity, obtained from the Vreman [41] model using a constant $c_k = 0.1$. The same single-value constant has been used in previous studies and it is also retained here [42–44].

2.1.4. Turbulence-chemistry interaction

In order to account for turbulence/chemistry interactions at the subgrid scale, the tabulated properties ψ from the manifold are integrated with a presumed-shape probability density function (PDF) that describes the statistical effect of turbulence on the flame structure [40]. Therefore, for any tabulated variable ψ this three-dimensional manifold $\psi = \psi(Z, C, \mathcal{H})$ must be integrated with a filtered joint-PDF $\tilde{P}(Z, C, \mathcal{H})$ as:

$$\tilde{\psi}(Z, C, \mathcal{H}) = \int_0^1 \int_0^1 \int_0^1 \psi(Z, C, \mathcal{H}) \tilde{P}(Z, C, \mathcal{H}) dZ dC d\mathcal{H}. \quad (9)$$

The joint-PDF $\tilde{P}(Z, C, \mathcal{H})$ of three independent variables is prohibitively complex for most modeling strategies, thus the joint-PDF is treated as a product of statistically independent PDFs of each degree of freedom [45]:

$$\tilde{P}(Z, C, \mathcal{H}) \approx \tilde{P}_Z(Z) \tilde{P}_C(C) \tilde{P}_H(\mathcal{H}). \quad (10)$$

In the present non-premixed turbulent combustion model, presumed shape PDFs are employed for each control variable. Both mixture fraction and progress variable distributions are characterized by β -functions, defined by the filtered values \tilde{Z} , \tilde{Y}_c and subgrid variances $Z_v = \tilde{Z}\tilde{Z} - \tilde{Z}\tilde{Z}$, $Y_{c,v} = \tilde{Y}_c\tilde{Y}_c - \tilde{Y}_c\tilde{Y}_c$ of Z and Y_c , respectively. Meanwhile, a δ -function is applied to the scaled enthalpy. This modeling strategy assumes that most unresolved effects are attributed to spatial mixture fraction and progress variable fluctuations.

A closure for the subgrid scale variances Z_v , $Y_{c,v}$ is then required to recover the tabulated quantities, so transport equations for Z_v and $Y_{c,v}$ are solved in this study [46] on top of Eqs. (7) and (8). The transport equations for the mixture fraction and progress variable subgrid variances are given by:

$$\frac{\partial \bar{\rho} Z_v}{\partial t} + \nabla \cdot (\bar{\rho} \tilde{\mathbf{u}} Z_v) = -\nabla \cdot \bar{\tau}_{Z_v} + \nabla \cdot (\bar{\rho} \bar{D} \nabla Z_v) - 2\bar{\tau}_Z \cdot \nabla \tilde{Z} - 2\bar{s}_{ZZ}, \quad (11)$$

$$\frac{\partial \bar{\rho} Y_{c,v}}{\partial t} + \nabla \cdot (\bar{\rho} \tilde{\mathbf{u}} Y_{c,v}) = -\nabla \cdot \bar{\tau}_{Y_{c,v}} + \nabla \cdot (\bar{\rho} \bar{D} \nabla Y_{c,v}) - 2\bar{\tau}_{Y_c} \cdot \nabla \tilde{Y}_c - 2\bar{s}_{YY_c} + 2 \left(\bar{Y}_c \bar{\omega}_{Y_c} - \tilde{Y}_c \bar{\omega}_{Y_c} \right). \quad (12)$$

The unresolved fluxes of mixture fraction and progress variable variances, $\bar{\tau}_{Z_v}$ and $\bar{\tau}_{Y_{c,v}}$, are closed using a gradient diffusion approach, while the unresolved part of the scalar dissipation rate of mixture fraction and progress variable, \bar{s}_{ZZ} and \bar{s}_{YY_c} respectively, are required. These terms are modeled assuming a linear relaxation of the variance within the subgrid [40] and are given by:

$$\bar{s}_{ZZ} = -\bar{\rho} \frac{Z_v}{\tau_{SGS}}, \quad (13)$$

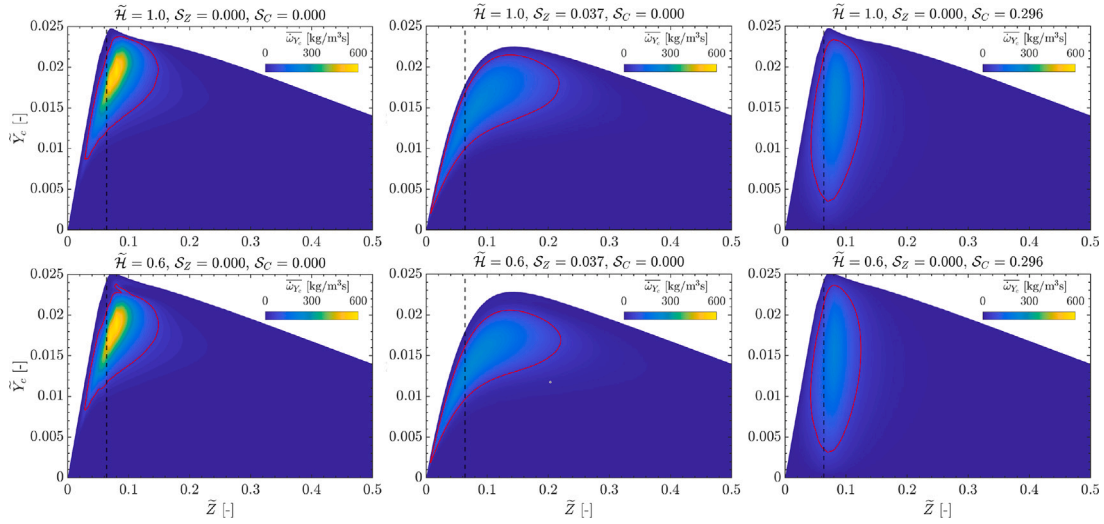


Fig. 1. Illustration of the non-adiabatic manifold. Effect of scaled enthalpy \tilde{H} , mixture fraction segregation factor \tilde{S}_Z and progress variable segregation factor \tilde{S}_C on the $\tilde{Z} - \tilde{Y}_c$ map of the filtered progress variable source term $\overline{\omega_{Y_c}}$. Red line: isoline of $\overline{\omega_{Y_c}} = 60$ kg/m³s (~10% max.). (For interpretation of the references to color in this figure legend, the reader is referred to the web version of this article.)

$$\bar{s}_{Y_c} = -\bar{\rho} \frac{Y_{c,v}}{\tau_{SGS}}. \quad (14)$$

where τ_{SGS} is a sub-grid time scale [42]. The chemical state of the turbulent flame in the LES framework is ultimately described by the five control variables: \tilde{Z} , Z_v , \tilde{Y}_c , $Y_{c,v}$ and \tilde{h} .

The thermochemical table contains $81 \times 7 \times 81 \times 7 \times 6$ entries corresponding those five control variables. For the progress variable discretization, a power function is used considering an exponential value of 3, while the mixture fraction space is discretized with a non-uniform distribution centered at the stoichiometric point. Mixture fraction and progress variable variances are also discretized with a power function, using a value of 3 for the exponent. The enthalpy level is tabulated for 6 equidistant steps. Note, that the number of these levels is larger than the number of different radiation scalings applied, we chose this approach because the radiation scaling does not guarantee an equidistant spacing in enthalpy, thus more levels are applied in the table to represent the flamelets in sufficient detail.

Different $\tilde{Z} - \tilde{Y}_c$ maps of the filtered progress variable source term are illustrated in Fig. 1 as function of the scaled enthalpy \tilde{H} , mixture fraction variance and progress variable variance. Note that variances are represented here by the corresponding segregation factor: $S_Z = \frac{Z_v}{\tilde{Z}(1-\tilde{Z})}$ and $S_C = \frac{C_v}{\tilde{C}(1-\tilde{C})}$. In general, the progress variable source term is affected by variations of the three control variables. Although $\overline{\omega_{Y_c}}$ peak value is not significantly affected by enthalpy, it is displaced to lower \tilde{Y}_c values when decreasing \tilde{H} . On the other hand, the effect of mixture fraction and progress variable subgrid variances is generally more relevant, since both considerably reduce the source term peak and distribute the values of $\overline{\omega_{Y_c}}$ along the respective coordinate. In addition, S_Z affects the \tilde{Y}_c profile, reducing and moving the peak to higher mixture fraction while widening the region of relevant progress variable source terms.

2.2. Soot modeling strategy

2.2.1. Sectional soot model

The soot modeling approach employed in the present work is based on the discrete sectional method (DSM) [17,47]. In the DSM-based models, soot particle volume ranges are divided into a n_{sec} finite number of sections. For each representative soot size (section i), the governing equation for the soot mass fraction $Y_{s,i}$ is solved by considering flow convection, diffusion, thermophoresis, and soot sources. The

sectional soot transport equation can be formulated as:

$$\frac{\partial(\rho Y_{s,i})}{\partial t} + \nabla \cdot (\rho[\mathbf{u} + \mathbf{v}_T] Y_{s,i}) = \nabla \cdot (\rho D_s \nabla Y_{s,i}) + \dot{\omega}_{s,i} \quad \forall i \in [1, n_{sec}] \quad (15)$$

where \mathbf{v}_T , D_s , $\dot{\omega}_{s,i}$ denote thermophoretic velocity (calculated with Friender's [48] expression), soot diffusion coefficient (assumed to be constant for all particle sizes), and sectional source term, respectively. The source terms for soot chemistry are evaluated by including the contributions of soot kinetics (nucleation, PAH condensation, surface growth, oxidation) and soot particle dynamics (coagulation) sub-processes. Soot is assumed to nucleate through the dimerization of PAH, taken as Pyrene (A4) in the current model. The condensation process is modeled as the coalescence of a PAH molecule on the surface of soot particles. The growth and oxidation of soot particles by surface reactions are modeled through the standard hydrogen-abstraction-C₂H₂-addition (HACA) mechanism [49,50]. The strategy introduced by Hoerlle and Pereira [51] is used to account for the conservation of surface radicals during acetylene addition. The coagulation process of soot particles is described by following the model proposed by Kumar and Ramkrishna [52]. The morphological description of soot particles is not considered for simplicity. A detailed description of the soot model can be found in [51]. This soot modeling approach has been extensively validated in laminar flames in previous works [51,53].

2.2.2. Description of the FGM-CDSM formalism for LES

In the present FGM-CDSM approach, the detailed chemistry-based solutions of steady and unsteady adiabatic counterflow diffusion flamelets are used for the creation of the manifold. During flamelet generation, transport equations for soot mass fractions in n_{sec} sections are also solved. However, for the application of the discrete sectional method in LES, filtered transport equations are solved for the soot mass fraction in a few n_c clustered sections instead n_{sec} as:

$$\frac{\partial \bar{\rho} \tilde{Y}_{s,j}^c}{\partial t} + \nabla \cdot (\bar{\rho}[\tilde{\mathbf{u}} + \tilde{\mathbf{v}}_T] \tilde{Y}_{s,j}^c) = \nabla \cdot \left[\bar{\rho} \left(\tilde{D}_s + \frac{v_t}{S_C} \right) \nabla \tilde{Y}_{s,j}^c \right] + \tilde{\omega}_{s,j}^c \quad \forall j \in [1, n_c] \quad (16)$$

By assuming the preservation of soot PSD within the clustered section, the soot mass fraction in a clustered section ($\tilde{Y}_{s,j}^c$) is given by:

$$\tilde{Y}_{s,j}^c = \sum_{i=j^{\min}}^{j^{\max}} \tilde{Y}_{s,i} \quad (17)$$

where i_j^{\min} and i_j^{\max} are, respectively, the lower and upper limit of the sections i that are clustered in j . The thermophoretic velocity \tilde{v}_T in Eq. (16) is modeled following [54]:

$$\tilde{v}_T = -0.554\bar{v} \frac{\nabla \tilde{T}}{\tilde{T}}. \quad (18)$$

In the current modeling approach, soot source terms are tabulated in the manifold. Hence, the non-linear dependence of different soot subprocesses with sectional soot mass fractions is not explicitly solved by the governing equations, but included in the flamelet computations. The inter-sectional dependence of soot particles is implicitly accounted for in the flamelet stage, where a full description of the gas phase and soot sectional equations are solved fully coupled [38]. Therefore, the resulting flamelet calculation accounts for all the soot sub-processes and the inter-sectional dependency. This method allows for a reduction in computational cost by the clustering of the soot sections, which mainly assumes that the interactions of the clustered sections with the turbulent flow field is similar to those of the individual sections [19].

The approach employed for the chemical source term treatment in the transport of slowly evolving species such as PAH and NO in other works [10,45], is applied for soot in the proposed modeling framework [19]. Accordingly, the soot source term for the clustered section is split into production ($\dot{\omega}_{s,j}^{c,+}$) and consumption rates ($\dot{\omega}_{s,j}^{c,-}$). The consumption rate is linearized by soot mass fraction to avoid the un-physical production of soot, so the filtered soot source term for the clustered section is modeled as:

$$\bar{\omega}_{s,j}^c = \bar{\omega}_{s,j}^{c,+} + \bar{\omega}_{s,j}^{c,-} \approx \left[\bar{\omega}_{s,j}^{c,+} \right]^{\text{tab}} + \tilde{Y}_{s,j} \left[\frac{\dot{\omega}_{s,j}^{c,-}}{Y_{s,j}} \right]^{\text{tab}}, \quad (19)$$

where the production term and linearized consumption term are parameterized through gas-phase thermochemical variables and tabulated (denoted by 'tab' superscript) in the manifold. For the LES application, the soot source term is convoluted with the β -PDF function in a pre-processing stage. With this approximation, turbulence-soot interaction is partially accounted for by including the effect of sub-grid scale fluctuations in mixture-fraction and progress variables to the soot source terms.

After the transport of the clustered sections, the distribution of soot mass fraction within the n_{sec} sections is re-constructed ($Y_{s,i}^{re}$) via the expression:

$$\tilde{Y}_{s,i}^{re} = \left[\tilde{F}_i \right]^{\text{tab}} \tilde{Y}_{s,j}^c \quad \forall j \in (1, n_c) ; i \in (1, n_{sec}), \quad (20)$$

with F_i being the mass fraction of section i in cluster j given by:

$$F_i = \frac{Y_{s,i}}{\sum_{t=i_j^{\min}}^{i_j^{\max}} Y_{s,t}}. \quad (21)$$

This fraction is assumed to be a function of the control variables only and it is included in the database. Subsequently, relevant soot quantities such as total number density, average particle diameter, and PSDF can be derived from the re-constructed soot mass fractions using the appropriate relations [51].

In this work, 60 original soot sections are considered during the manifold generation, which are grouped into 6 clusters for the efficient application of the model in the LES. This 90% reduction in sectional dimensions provided a speed-up factor of 4.5 in laminar 2-D flames with almost no impact on soot predictions [19], and it has been retained in this application.

2.3. Numerical methods

The discretization strategy is based on a conservative finite element scheme, where stabilization is only introduced for the continuity equation by means of a non-incremental fractional-step method, modified in

order to account for variable density flows [42]. The final scheme preserves momentum and angular momentum for variable density flows. The error of kinetic energy conservation is of order $O(dt \cdot h^{k+1})$, thus dissipation is limited. Standard stabilized finite elements are used for the scalars, while the time integration is carried out by means of an explicit third order Runge-Kutta scheme for momentum and scalars. The chosen low dissipation FE scheme presents good accuracy compared to other low dissipation finite volume and finite difference methods with the advantage of being able to increase the order of accuracy at will without breaking the fundamental symmetry properties of the discrete operators. The proposed modeling and numerical framework has been developed in the multiphysics code Alya [55].

3. Test case description

3.1. Experimental setup

The pressurized ethylene-based model combustor from DLR is studied in this work. It exhibits features similar to real gas turbine burners and it is representative of the RQL concept. A more detailed description of the experimental setup can be found in the work of Geigle et al. [22, 23].

A sketch of the geometrical burner characteristics is shown in Fig. 2(a). The burner contains a dual radial swirler configuration for the air supply. The inner swirler consists of 8 vanes, while the outer one is composed of 11 ducts. The combustion chamber has a square section of $68 \times 68 \text{ mm}^2$ and a height of 120 mm. Up to four quartz windows are arranged on the sides of the chamber ensuring the optical access for measurements. Additional ducts for secondary oxidation air injection are located at the corners of the chamber, 80 mm downstream the chamber inlet plane. Fuel is injected through a concentric ring of 60 equally spaced ports located between the inner and outer air inlets.

Multiple experimental diagnostics are available at several operating points for flame characterization and soot formation [22,23,56]. Velocity component statistics at different positions inside the combustion chamber were measured using Stereo-Particle Image Velocimetry (Stereo-PIV). Temperature measurements were obtained from Coherent Anti-Stokes Raman scattering (CARS) and OH radical distribution was qualitatively estimated by Laser Induced Fluorescence (LIF). In addition, Planar Laser-Induced Incandescence (LII) was used to measure the soot volume fraction.

3.2. Numerical setup

The computational domain considered for numerical simulations is based on the experimental test rig described in the previous subsection. It includes all the different components of the burner: inlet ducts for air and fuel supply, the dual swirler injection system, the combustion chamber and secondary oxidation air ducts, while the fuel injection is modeled as a single continuous ring. Furthermore, the domain includes a cubic volume of side 400 mm at the exit of the burner to reproduce the atmosphere.

In this study, two operating conditions are evaluated: the reference case including secondary oxidation air (Op 1) and the configuration without secondary jets (Op 2). A summary of the flame parameters is presented in Table 1. Similar meshes of 52M (Op 1) and 48M (Op 2) elements are used for this geometry with the difference in mesh size is given to the refinement region of the dilution jets. Fig. 2(b) shows a representation of the computational domain and an overview of the mesh for Op 1. They are composed mainly of tetrahedrons, prisms and pyramids and a minimum filter size of $\Delta x = 0.15 \text{ mm}$ ($\Delta x = \sqrt[3]{V_{cell}}$, where V_{cell} is the cell volume) is considered for the refinement of the near mixing region inside the combustion chamber and 0.05 mm within the fuel injector. Layers of prisms are applied in the air and fuel ducts in order to better resolve the boundary layer. Concerning the mesh quality, Pope's criterion [57] is fulfilled and over 80% of the turbulent

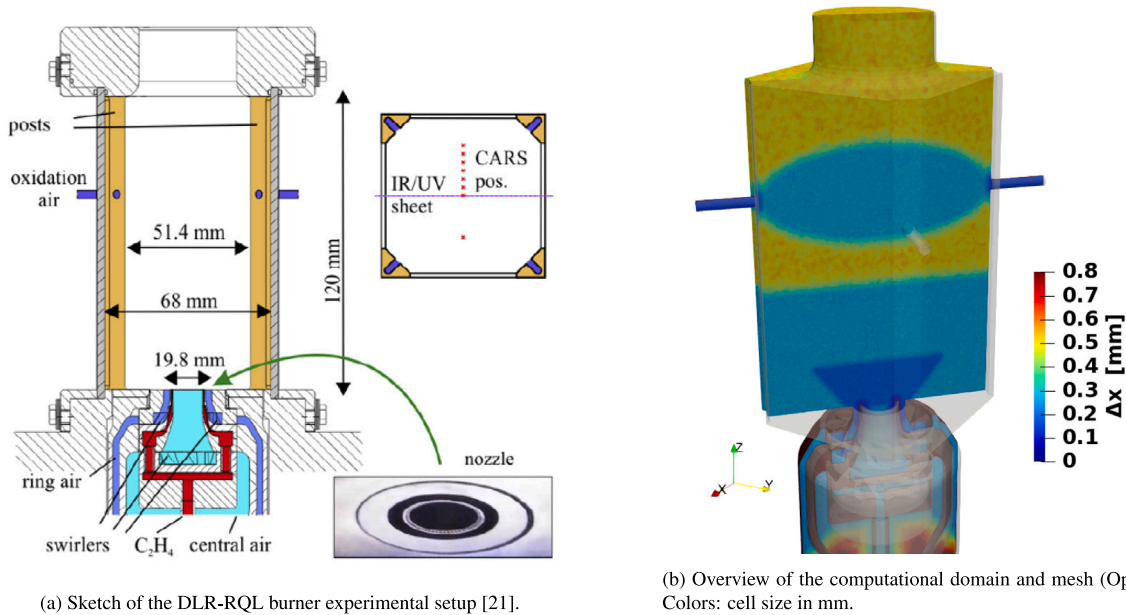


Fig. 2. Schematics of the experimental and numerical configurations of the DLR burner.

Table 1

Flame parameters of the operating conditions evaluated.

	p [bar]	ϕ_{global} [-]	Q_a [slpm]	$Q_{a,ox}$ [slpm]	T_a [K]	Q_f [slpm]	T_f [K]
Op 1	3	0.86	468.3	187.4	300	39.3	300
Op 2	3	1.2	468.3	0	300	39.3	300

Pressure, p ; global equivalence ratio, ϕ_{global} ; mass flows for air through burner, Q_a ; oxidation air through secondary inlets, $Q_{a,ox}$; fuel, Q_f ; air and fuel temperatures, T_a and T_f .

kinetic energy is resolved in almost the entire combustion chamber. In addition, different meshes were used to check grid convergence, however, further refinements did not affect significantly the results.

Constant air and fuel mass flow rates at 300 K are prescribed as inlet conditions. Regarding wall boundary conditions, both non-slip adiabatic and isothermal walls are used. The combustion chamber wall temperature is specified according to the experimental measurements of the quartz windows [58].

In this work, time-averages for flow statistics are collected over approximately 5 flow-through times to allow for the soot to reach steady state. The flow-through is estimated by the averaged axial velocity integrated over the combustion chamber volume.

4. Results

This section includes the numerical results of the DLR-RQL burner using Large-Eddy Simulations. First, velocity and temperature fields are presented in order to evaluate the capabilities of the current approach to capture the gas phase. Subsequently, the results of Soot Volume Fraction (SVF) and Particle Size Distribution (PSD) are shown and soot formation and oxidation predictions using the FGM-DSM modeling framework are discussed. The configuration including secondary air injection (Op1) is taken as a reference for results, and the impact of removing the secondary jets is evaluated in the last subsection.

Two different simulations are considered to investigate the effect of heat losses: one case employs adiabatic walls and a manifold composed of adiabatic flamelets while another case includes isothermal walls and a non-adiabatic manifold (Adiabatic and Non-adiabatic in legends, respectively).

4.1. Gas phase assessment

Instantaneous and time-averaged axial velocity contours are presented in Fig. 3 to show a qualitative description of the flow field and turbulent structures. Velocity results are only presented for the non-adiabatic simulation, since the velocity field is not strongly affected by the heat loss to the walls. Zero-axial velocity isoline is represented with the white isoline to identify the recirculation regions. In general, the current LES is able to capture the characteristics of the swirling flow in this configuration. A corner recirculation region (CRZ) is located at the outer bottom part of the combustion chamber, close to the air and fuel injection. In addition, an inner recirculation zone (IRZ) is formed at the central part of the combustor, where axial velocity reaches its minimum negative value. Due to the presence of the secondary oxidation jets, the axial velocity field is strongly affected downstream, at 80 mm in the axial direction, approximately. Part of this secondary air is recirculated upstream, affecting the local mixture field in the combustion region, and contributing to soot oxidation, as will be discussed later.

Fig. 4 shows the comparison between the numerical results and experimental data for the time-averaged and Root Mean Square (RMS) velocity components at the centerline and at different axial stations inside the combustion chamber (see Fig. 3 left). At the centerline, two datasets are included concerning the treatment of experimental measurements: Field of View (FoV) and Sum of Correlation (SoC) data [56]. The recirculation pattern described previously is clearly observed along the burner axis (see Fig. 4(a)), where axial velocity remains negative until the secondary jets axial position (80 mm). In addition, the widening of swirled jets is properly captured by LES, as it is observed from the axial component at stations presented in Fig. 4(c). Radial and tangential velocity components are also illustrated in fig 4(e) and 4(g). As for axial velocity, some discrepancies appear at radial positions over ~ 10 mm close to the injector, but the differences vanish downstream. In terms of velocity fluctuations, RMS is also properly captured both at the centerline and at the stations and only small discrepancies are found near the injection plane and close to the location of the dilution air. The overall agreement with the experimental measurements is satisfactory and the velocity field is accurately reproduced by numerical simulations.

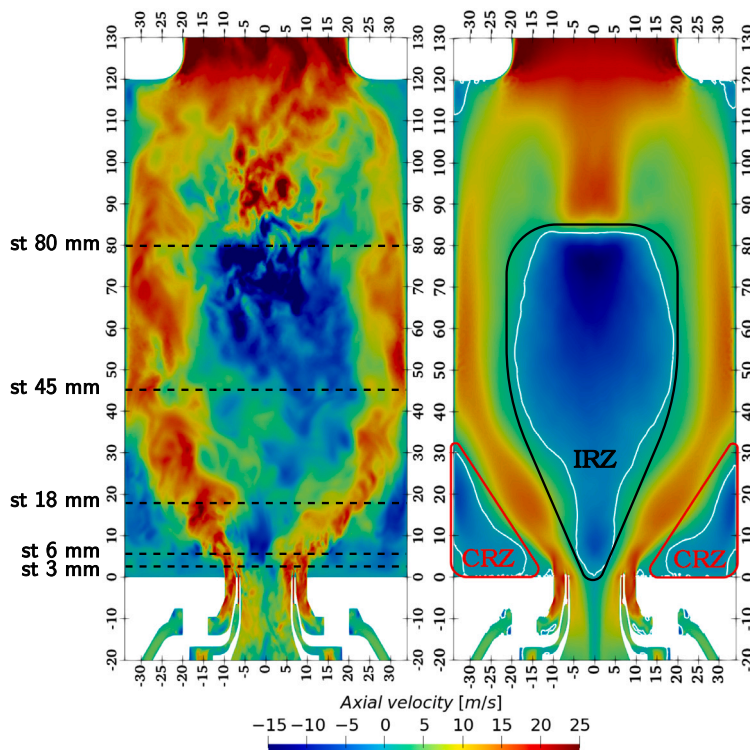


Fig. 3. Instantaneous (left) and time-averaged (right) axial velocity. White line corresponds to the zero axial velocity isoline. Spatial units in mm. (For interpretation of the references to color in this figure legend, the reader is referred to the web version of this article.)

The temperature field is illustrated in Fig. 5, where both adiabatic and non-adiabatic numerical results are presented in order to assess the effect of heat loss in this combustor. In addition, the scaled enthalpy contour is presented on the right panel to identify the regions more affected by this effect. As observed, the temperature value is quite similar between both approaches in most of the rich region enclosed by the stoichiometric mixture fraction isoline (white) and also in the IRZ. However, the effect of heat losses is particularly noticeable near the combustion chamber walls and in the CRZ. Inside this region, with longer residence time, the effect of the non-adiabatic walls is more prominent, and lower temperatures are predicted. Fig. 6 shows a quantitative comparison between LES and experimental temperature values at different axial stations and on the centerline. In general, a good prediction of the reacting flow is achieved in view of the mean and RMS temperature results. Strong temperature gradients can be observed close to the shear layers that separate both recirculation regions, and the simulations properly capture the decrease of temperature in the central region due to the cold secondary flow. However, the temperature fluctuation is overpredicted at the first axial positions close to the burner axis, where the flame base is located. At further radial positions, which are affected by the CRZ, the agreement with the experimental data is remarkably better when considering the non-adiabatic approach in terms of both mean and RMS temperature. Notice that this configuration is more consistent with the flow conditions in the burner, where enthalpy is affected by heat loss, and the manifold is able to account for this effect on the reaction rates, see Fig. 1. In view of the results presented in this section, the proposed modeling approach based on non-adiabatic counterflow diffusion flamelets is able to reproduce the flow conditions in this configuration. Therefore, the following section will be focused on the capabilities of the LES-FGM-CDSM framework to predict soot formation and oxidation in turbulent flow conditions and moderate pressure.

4.2. Soot predictions

This subsection contains the results for soot formation obtained using the FGM-DSM modeling approach for the DLR-RQL burner configuration with secondary oxidation air. First, the comparison between the numerical SVF field and the experimental measurements is presented. Then, the soot formation and oxidation processes are analyzed. Finally, Particle Size Distribution functions retrieved from the sectional method for soot are discussed.

4.2.1. Soot volume fraction assessment

A qualitative comparison of SVF fields can be observed in Fig. 7, in which the results with and without heat losses are included. For both cases, the spatial localization of soot is correctly predicted, although the onset of soot is located upstream of the experimental data for the adiabatic case, and accuracy is improved when accounting for heat losses. Soot is primarily present in the rich branches between the IRZ and the CRZ, and persists downstream in the combustor outer region while it is oxidized in the lean IRZ region due to secondary air injection.

In order to have a more quantitative evaluation of soot magnitude, Soot Volume Fraction profiles at different radial stations are illustrated in Fig. 8. Both modeling approaches show a considerably good prediction of SVF magnitude. Nevertheless, the adiabatic case presents a slightly higher overall soot level and an overestimation of the SVF peak. Taking into account that the soot main location (approximately between $-20 < x < 20$ mm and $10 < z < 25$ mm) is not much affected by the enthalpy loss, a strong variation on the soot field is not expected. In fact, the heat loss effect on SVF is more noticeable where CRZ affects flame temperature and thus precursors and soot chemistry, as shown in SVF profiles at $z = 18$ mm. The impact is limited downstream, where soot regions are subjected to low enthalpy losses. For reference, the regions more affected by heat loss effects

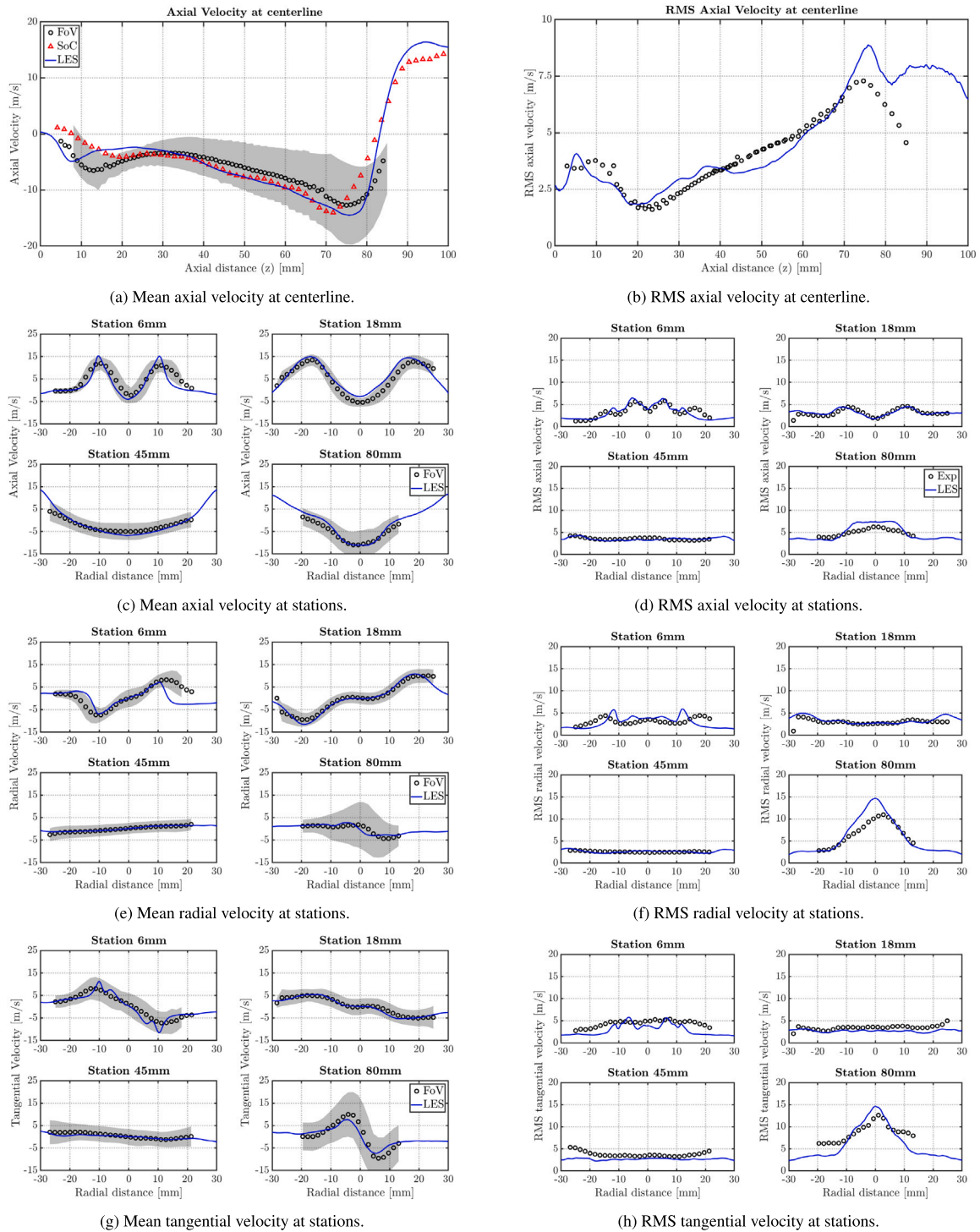


Fig. 4. Comparison between LES results (non-adiabatic case) and experiments of velocity field. Shaded area: RMS velocity fluctuation from FoV experiments.

may be derived from the temperature field in Fig. 5. Furthermore, the decrease on the peak value obtained when including wall heat losses is consistent with the conclusions of previous modeling works in this regard [31,59,60], where lower enthalpy levels decrease temperature and soot formation rate.

4.2.2. Analysis of soot formation and oxidation

A detailed analysis of the main mechanisms involved in soot formation and oxidation processes inside the combustor is addressed to evaluate the prediction capabilities of the proposed modeling approach.

The results presented in this subsection correspond to the case with secondary air injection using the non-adiabatic manifold, which is taken as a reference. Fig. 9 shows scattered plots of mixture fraction (\tilde{Z}) and temperature (\tilde{T}), colored by SVF (Fig. 9(a)) and the total soot source term $\tilde{\omega}_s^c$ (Fig. 9(b)). Note that the total soot source term corresponds to the sum of the source terms for clustered sections, according to Eq. (19), $\tilde{\omega}_s^c = \sum_{j=1}^{n_c} \tilde{\omega}_{s,j}^c$. Additionally, solid colored lines are overlapped on the plots representing different regions of the burner (R1 the near nozzle mixing layer region; R2 the rich outer branches; R3 the IRZ), which are depicted in Fig. 9(c). The scattered data is

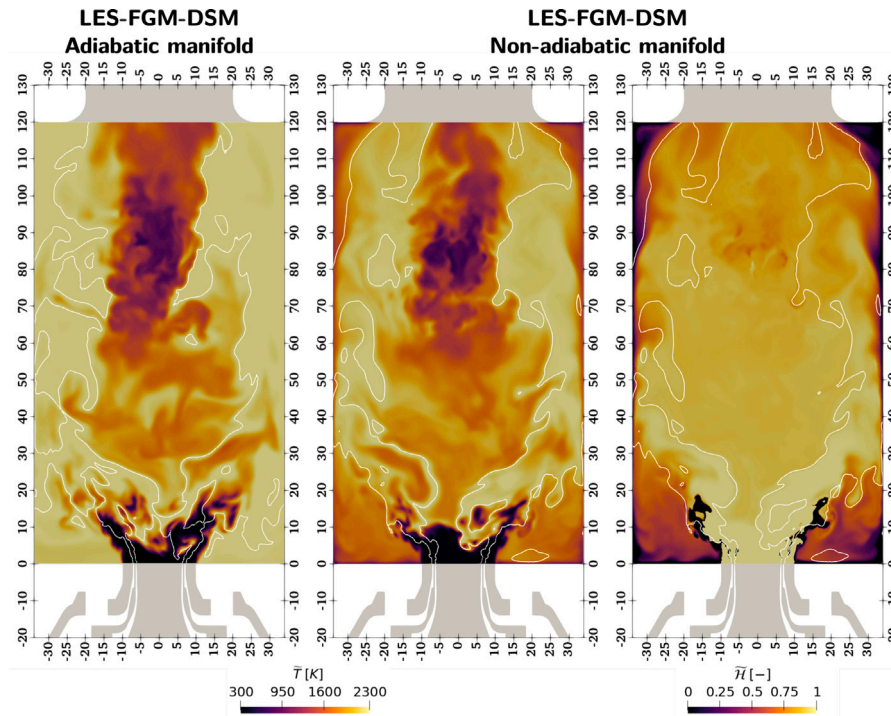


Fig. 5. Non-adiabatic effects on temperature field. Left: adiabatic temperature, center: non-adiabatic temperature, right: non-adiabatic scaled enthalpy. White line: stoichiometric mixture fraction isoline. Spatial units in mm. (For interpretation of the references to color in this figure legend, the reader is referred to the web version of this article.)

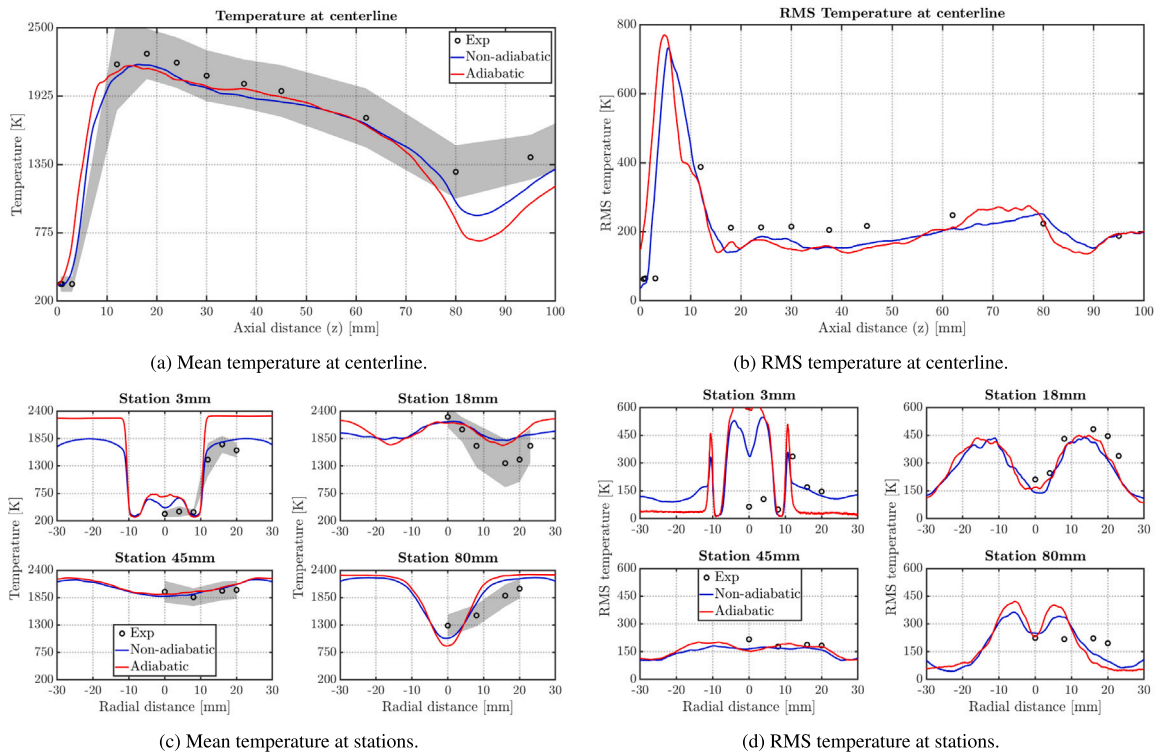


Fig. 6. Comparison between LES results (adiabatic and non-adiabatic) and experiments of temperature field. Shaded area: RMS of the measured temperature.

obtained from the instantaneous results in five different time instants including points inside the full combustion chamber with normalized enthalpy higher than 0.5 ($\tilde{H} > 0.5$) to avoid locations very close to the combustion chamber walls. Solid lines enclose the cloud of points associated with each region and they are conditioned to high scaled progress variable values ($\tilde{C} > 0.8$), in order to avoid non-representative

conditions for the soot analysis. As previously described in the SVF comparison, the highest soot quantity is mainly found in the mixture fraction rich side ($0.1 < \tilde{Z} < 0.2$) and high temperature ($\tilde{T} > 1500$ K). This location is mainly covered by R1 and to a lesser extent by R2, where the reactivity and rich mixture lead to high temperature and soot precursors concentrations. In view of Fig. 9(b), this \tilde{Z} range

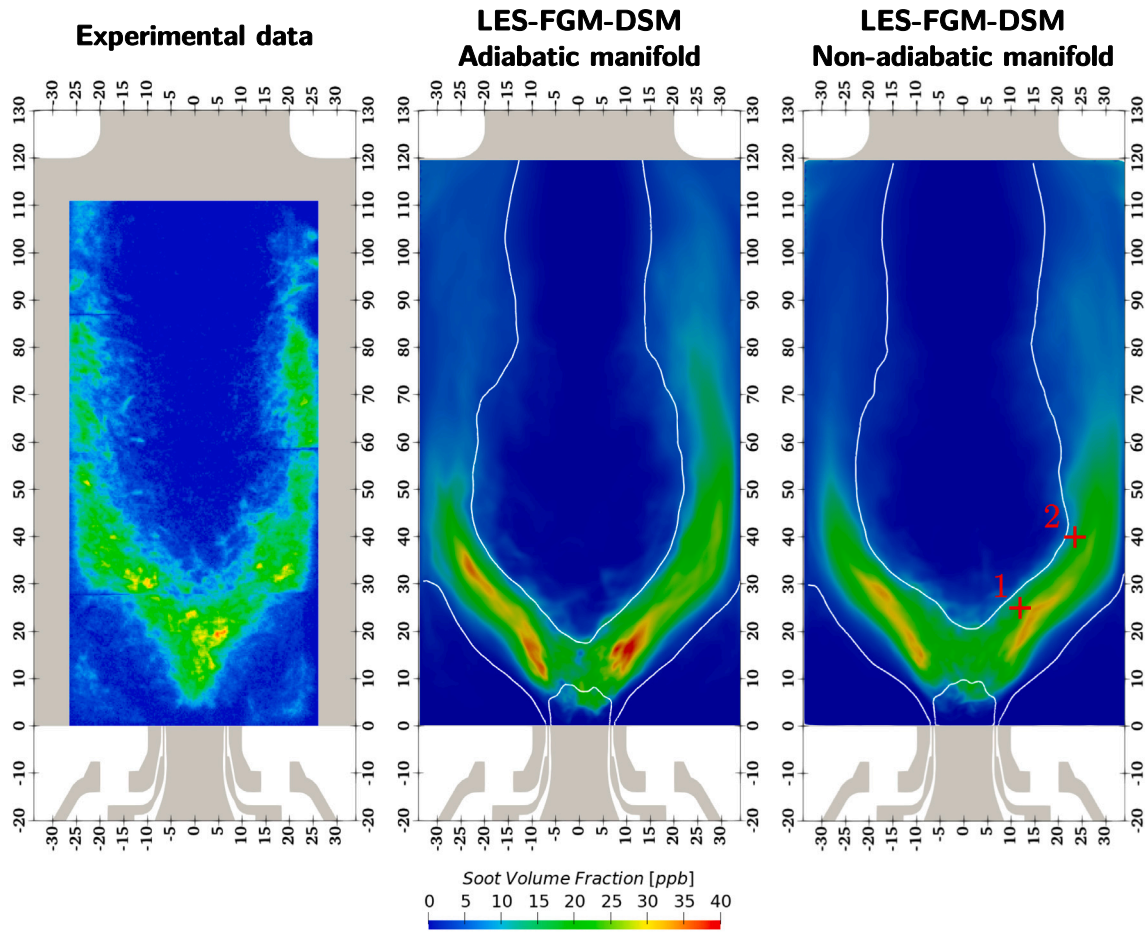


Fig. 7. Comparison of time-averaged Soot Volume Fraction (SVF) contours. White line: stoichiometric mixture fraction. Markers: points for time-averaged PSD computation 14. Spatial units in mm. (For interpretation of the references to color in this figure legend, the reader is referred to the web version of this article.)

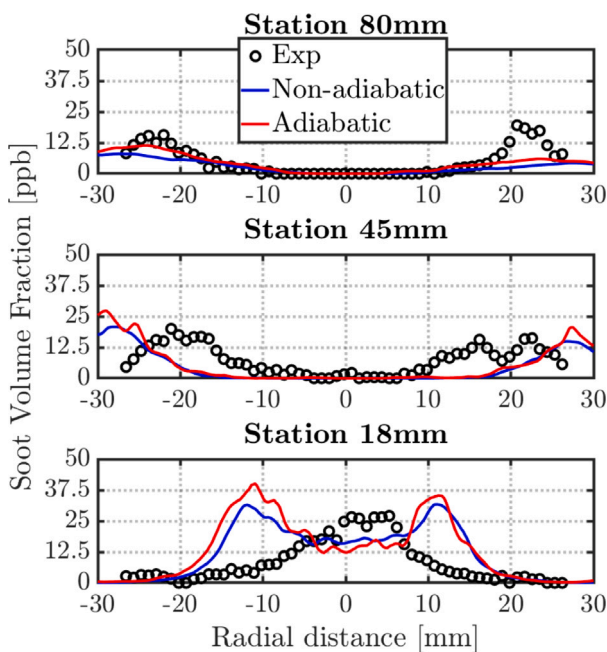


Fig. 8. Comparison between LES results (adiabatic and non-adiabatic) and experiments. Soot Volume Fraction (SVF) at different radial stations.

corresponds to the highest positive source terms values and, thus, the main soot production region. When \tilde{Z} approaches the stoichiometric condition (values below 0.1), $\tilde{\omega}_s^c$ reaches highly negative values and soot consumption eventually becomes predominant. Furthermore, contour lines make it possible to distinguish different states in each of the analyzed regions of the burner. R1 clearly evidences a wider range of thermochemical states from lean and low-temperature conditions due to the proximity to the injection system and the CRZ, to high-temperature rich regions characterized by soot production. R2 is more enclosed in high-temperature zones and a limited range of mixture fraction, where both soot production and consumption are present. Finally, R3, primarily corresponding to the IRZ, is extended to the lower temperature and lean conditions (and strong soot consumption) due to the secondary oxidation air.

The soot formation processes and variety of thermochemical conditions in each region may be further analyzed by means of Fig. 10. In this figure, scattered plots of the main control variables (\tilde{Z} and \tilde{Y}_c) colored by the joint-PDF of $\tilde{Z}-\tilde{Y}_c$ are illustrated for each region. A black contour line is also included, representing the boundary line that encloses the cloud of points with a significant soot production rate ($\tilde{\omega}_s^c > 0.05 \text{ kg/m}^3\text{s}$), in order to identify the presence in the soot formation area. Note that in this case the data is not conditioned to the scaled progress variable \tilde{C} .

A strong fluctuation in R1, especially in terms of \tilde{Y}_c , compared to the other regions is evidenced due to the multiple states present in this zone. Despite the most probable states being lean inert and slightly rich reacting conditions, a high probability of soot formation conditions is also observed for R1. On the other hand, R2 presents the

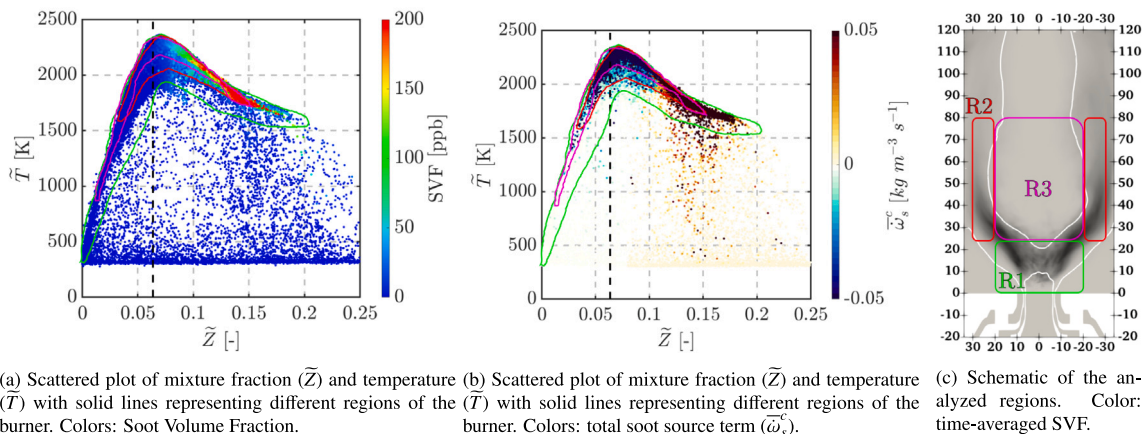


Fig. 9. Scattered plots of mixture fraction and temperature from instantaneous LES results.

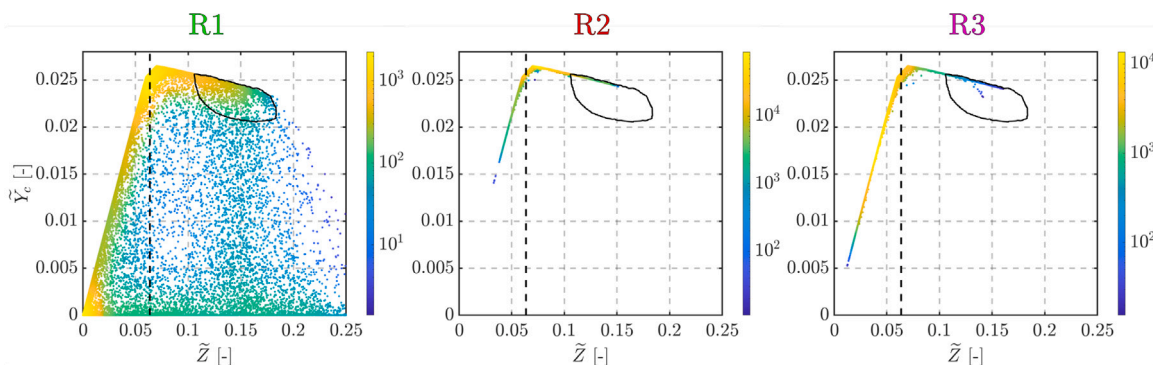


Fig. 10. Scattered plots of mixture fraction and progress variable from instantaneous LES results. Colors: joint-PDF of \tilde{Z} - \tilde{Y}_c . Black line: isoline of $\tilde{\omega}_s = 0.05 \text{ kg/m}^3 \text{ s}$.

highest probability in regions between soot formation and oxidation, consequently, soot is not completely oxidized and is transported and remains downstream. Finally, R3 is mainly located in lean conditions with strong soot oxidation term, therefore, a close to zero SVF value is observed.

In view of the most probable states derived from the joint-PDF in R1, an intermittent behavior of soot formation is suggested. Note that, although there is a high probability of finding suitable conditions for soot formation, it is even more common to find thermochemical states close to the stoichiometric, lean or inert conditions. In order to properly illustrate soot intermittency, Fig. 11 shows the scatter data of mixture fraction and SVF colored by the joint-PDF of \tilde{Z} -SVF. As observed, although very high SVF values are present within the range of $0.1 < \tilde{Z} < 0.15$, they are very rarely found, and the soot quantity is more likely to be low. In fact, the most probable situation is to find a very low (even close to zero) SVF magnitude and significant soot peaks are eventually observed if proper flow and mixing conditions for soot production are satisfied.

Due to the unsteady behavior of the swirled flow and the intermittency on the soot generation, it is interesting to analyze the time evolution of certain quantities to better understand the soot formation and oxidation processes. Therefore, instantaneous contours of pyrene (A4), acetylene (C_2H_2), SVF and the total soot source term ($\tilde{\omega}_s$) are represented at three time instants in Fig. 12. The stoichiometric mixture fraction isoline is shown in white while the black line represents different soot source terms depending on the contour: 20% of the maximum nucleation source term (represented in the A4 mass fraction field, since A4 is the species involved in soot nucleation), 20% of the maximum surface growth source term (represented in the C_2H_2 mass fraction field,

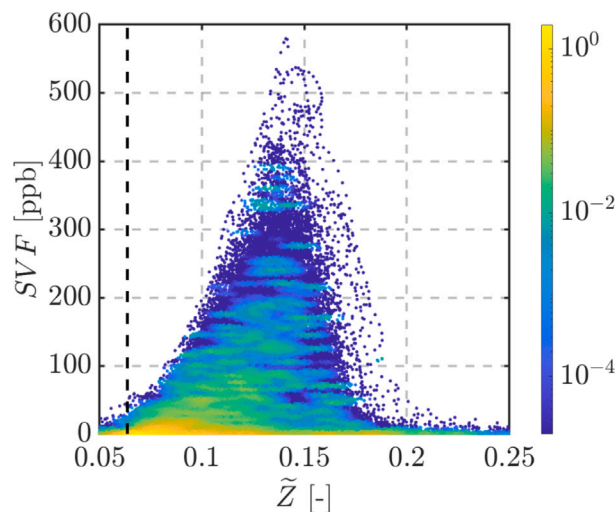


Fig. 11. Scattered plot of mixture fraction and SVF from instantaneous LES results. Color: joint-PDF of \tilde{Z} -SVF.

since it is involved in soot surface growth) and total soot source term equal to $-0.005 \text{ kg m}^{-3} \text{ s}^{-1}$ (represented in the SVF field). This particular temporal sequence clearly illustrates a complete soot formation event located along the right rich branch inside the combustor (red box in Fig. 12). The event starts with the formation of a rich-burned gas (RBG) pocket in the central near-nozzle region. Along the time sequence, this

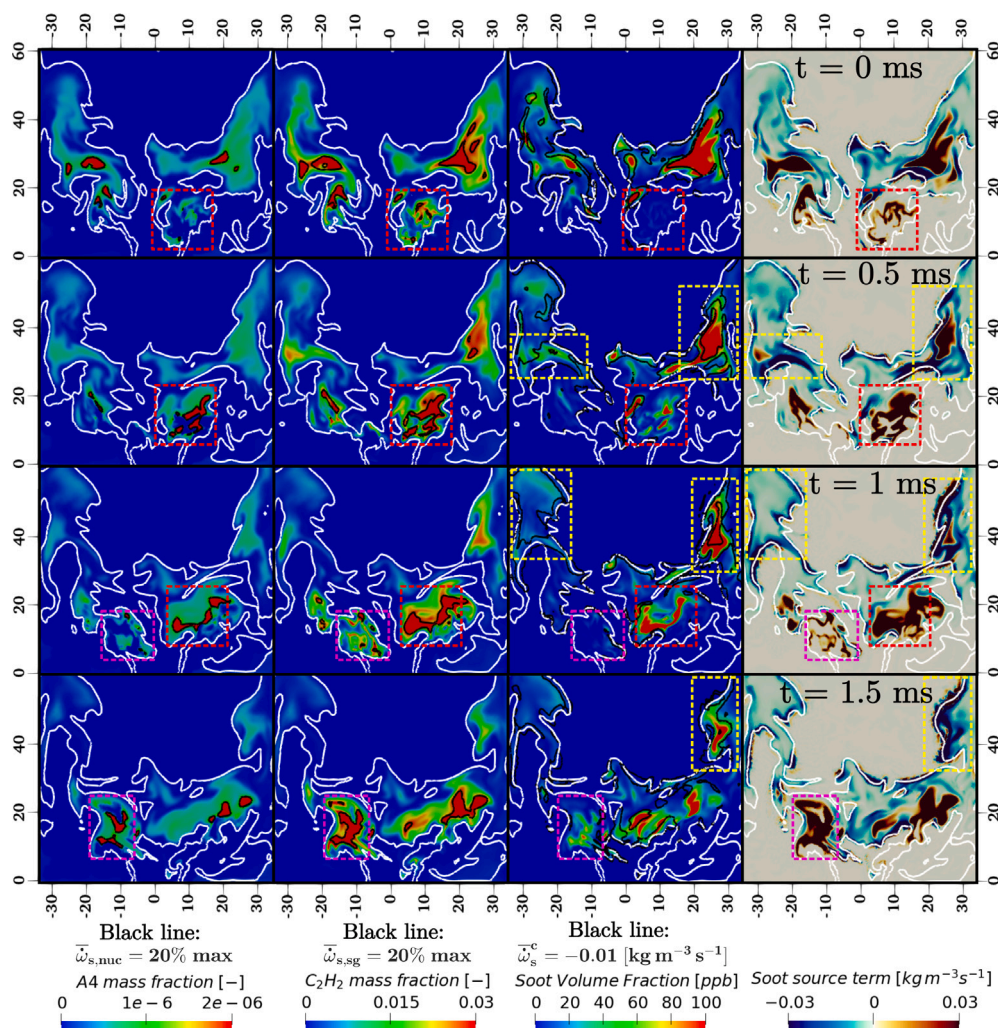


Fig. 12. Temporal sequence of A4 mass fraction, C_2H_2 mass fraction, SVF and soot source term contours. White line: stoichiometric mixture fraction isoline. Black lines: isolines of soot source terms. Spatial units in mm. (For interpretation of the references to color in this figure legend, the reader is referred to the web version of this article.)

pocket grows in size, and high concentrations of pyrene and acetylene are found inside ($x \sim 5$ mm and $z \sim 15$ mm). Consequently, soot inception and growth processes (black lines) are observed, which lead to a high positive total soot source term value and an increase in the SVF level (represented in the fourth and third, respectively). Note that the last two temporal frames ($t = 1$ and $t = 1.5$ ms) show the start of a new RBG pocket and soot formation event in the left branch (magenta box in Fig. 12, at $x \sim -10$ mm and $z \sim 15$ mm). Additionally, although A4 and C_2H_2 mass fraction peak values (and therefore nucleation and surface growth processes) are confined to the closer rich pockets, a higher C_2H_2 concentration is observed downstream and soot growth is still present along the slightly rich branches. On the other hand, soot oxidation events can be appreciated at locations closer to the stoichiometric mixture line. In Fig. 12, several oxidation sequences are clearly observed downstream at both branches (yellow boxes). Soot is formed, transported downstream and eventually approaches the IRZ, where lean-burned gas (LBG) with high OH concentrations is found. In these regions, high negative soot source terms are present and SVF decreases because of the fresh air coming from the secondary injection. The unsteady motion of RBG and LBG regions close to the injection nozzle is related to the flow dynamics induced by the secondary air

injection and these intermittent soot formation events reproduced by LES were experimentally observed by Stöhr et al. [61] and Litvinov et al. [62]. A video including a longer temporal sequence is provided in the Supplementary Material in order to complement the results shown in Fig. 12.

To illustrate the contributions of the soot subprocesses considered in the sectional modeling approach, time-averaged contours of the different source terms are presented in Fig. 13. In view of the magnitude of the source terms, soot production is mainly dominated by surface growth based on acetylene. In fact, soot surface growth magnitude is approximately one order of magnitude higher than the rest of the subprocesses. Regarding the spatial distribution, the most intense production (nucleation, PAH condensation and surface growth) terms are located at the main soot formation region described in previous figures, since the presence of A4, C_2H_2 and soot is quite important. It is worth mentioning that surface growth seems to be present in a slightly expended area, while nucleation and condensation are confined in the rich region close to the injection plane. A similar source term distribution inside the combustion chamber and trend for the different subprocesses can be observed in the works of Tardelli et al. [63] and Chong et al. [28] for the same combustor.

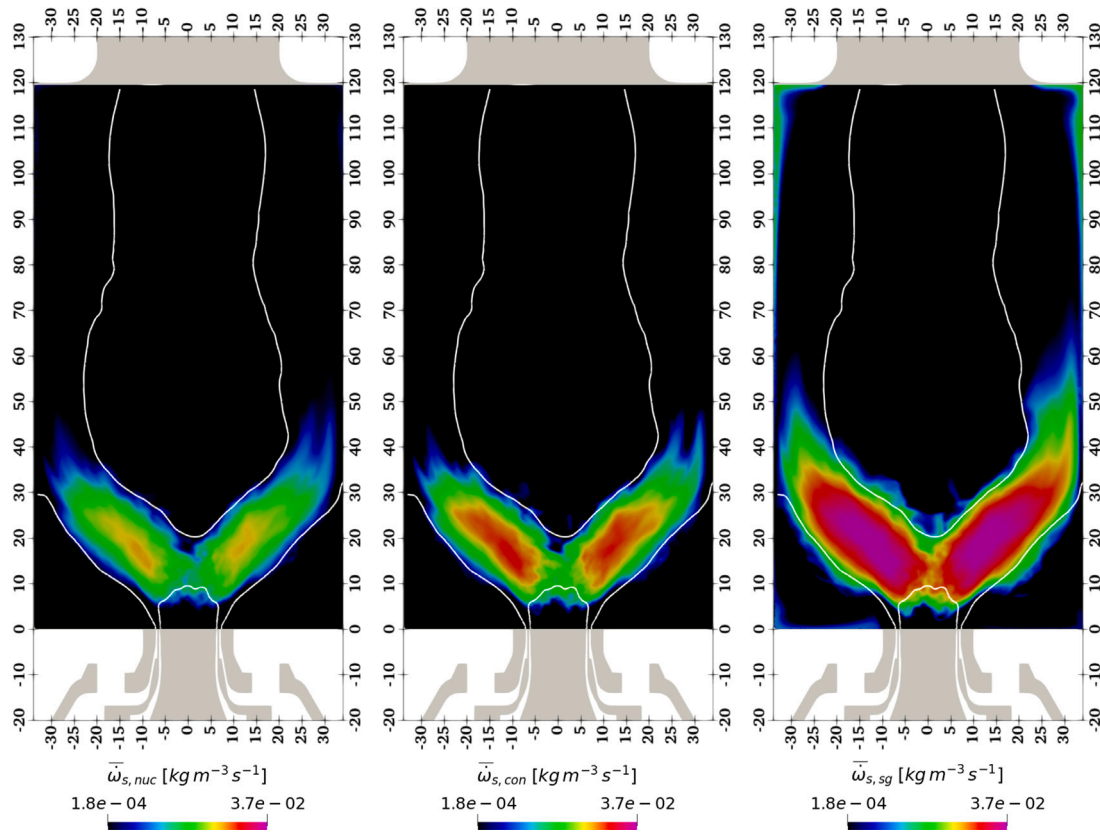


Fig. 13. Time-averaged contours of soot production source terms by subprocess. Left: nucleation. Center: condensation. Right: surface growth. White line: stoichiometric mixture fraction isoline. Legend in log scale. Spatial units in mm. (For interpretation of the references to color in this figure legend, the reader is referred to the web version of this article.)

4.2.3. Particle size distributions

Since the sectional method evaluated in this work provides information about particulate sizes, the Particle Size Distribution function (PSDF) has been computed at different locations inside the combustion chamber. For the analysis of size distributions, both temporal and spatial averaging of the function have been considered, using the original sections re-constructed from the different clusters (see Eq. (20) for additional details).

To evaluate the time evolution of the particle size distribution at specific coordinates, instantaneous and time-averaged PSDF are presented in Fig. 14. Two particular positions are selected for the analysis, whose location inside the combustion chamber can be observed in Fig. 7 (red markers). Point 1 ($x = 12$, $z = 25$ mm) is located near the main soot formation region while point 2 ($x = 24$, $z = 40$ mm) is found slightly downstream, following one of the rich branches. At each point, flow variables and soot clusters have been recorded during ≈ 4 ms of physical time. Regarding Fig. 14, the instantaneous (colored solid lines) and time-averaged (black dashed line) PSDF are presented on the left side. On the right-hand side, the time-evolution of filtered mixture fraction (\bar{Z}) and instantaneous SVF are recorded over the same time window as for the PSD computation. In any case, colors represent the instantaneous SVF. In view of the results, the point located close to the main soot formation region (1) reaches a higher mixture fraction value and, therefore, evidences a higher overall SVF magnitude. Although the relationship between SVF and mixture fraction is not instantaneous due to the delay induced by the transport equations for soot clusters, it is possible to observe how the amount of soot eventually increases when reaching high mixture fraction levels ($\bar{Z} > 0.1$ approximately).

Consequently, size distributions at this point evidence a high particle number that decreases at time instants when mixture fraction and soot quantity are slightly reduced. The second location (point 2) suggests a local fuel–air ratio closer to the stoichiometric conditions (\bar{Z} fluctuates around 0.08). In this case, soot is more affected by consumption processes and the SVF magnitude is generally lower. Therefore, the instantaneous function covers a lower range of particle number and the PSDF shape is slightly modified showing a strong reduction in the number of particles with small sizes.

Due to the dependency of the size distribution to the local mixture level observed in Fig. 14, it is interesting to perform a spatial averaging of the PSDF considering a certain amount of points conditioned to the mixture fraction, as presented in Fig. 15. A vertical cut plane of the burner colored by the total soot source term ($\bar{\omega}_s^c$) is shown on the left side to illustrate the different regions considered for the spatial average of the PSDF. Green and white lines represent the $\bar{Z} = 0.1$ and $\bar{Z} = Z_{st}$ isolines, respectively. Therefore, the green line encloses the primary soot production area while oxidation is mainly present in the region between the green and white lines (i.e. in the slightly rich zone near stoichiometric conditions, where soot is still present and oxidation is possible). The spatially averaged PSD functions in the two previously described regions are presented in the central plot. In view of the solid line (PSDF in the richer region), the domination of soot formation processes leads to a higher number of small particles and to a more almost uni-modal like PSDF shape. On the contrary, the PSDF computed in the zone closer to Z_{st} (dashed line) evidences an overall decrease in the number of particles of all sizes, strongly affecting the smallest diameters (up to 10 nm, approximately) which are easier to oxidize.

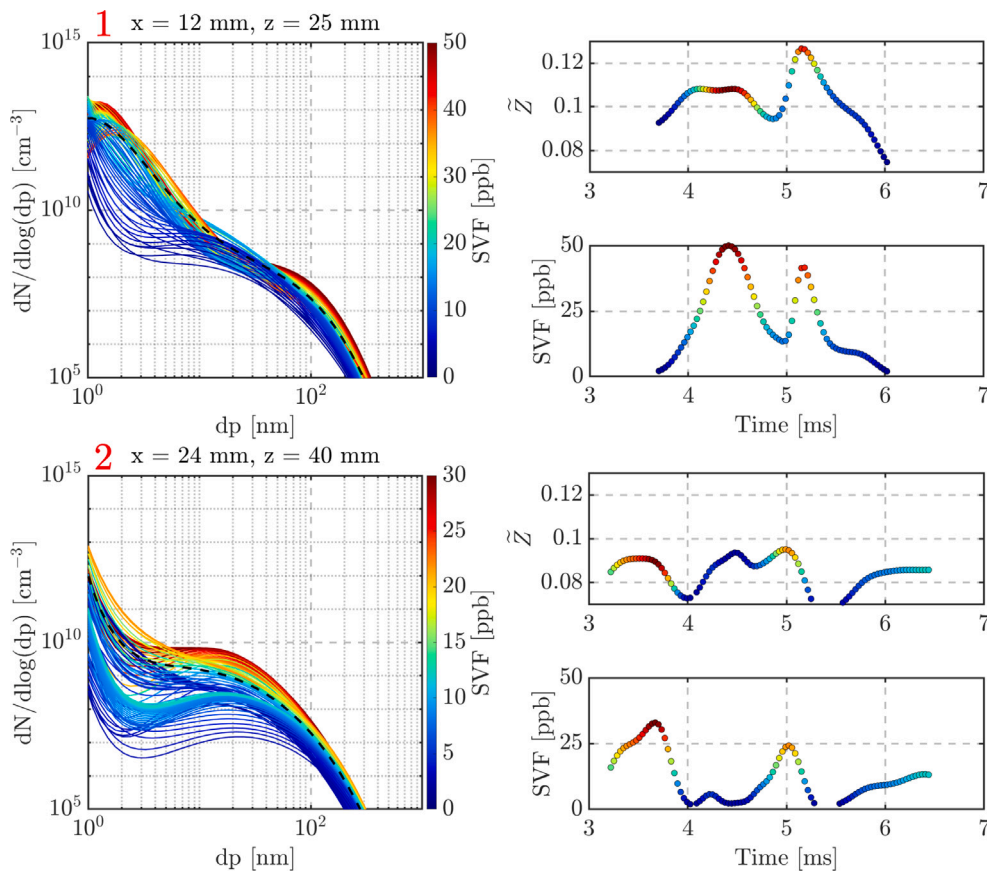


Fig. 14. Instantaneous and time-averaged PSD results (Op1) at two different locations inside the combustion chamber (see markers in Fig. 7). Left: instantaneous (solid lines) and time-averaged (black dashed line) PSDF. Right: time-evolution of mixture fraction (\bar{Z}) and SVF. Colors: instantaneous SVF magnitude.

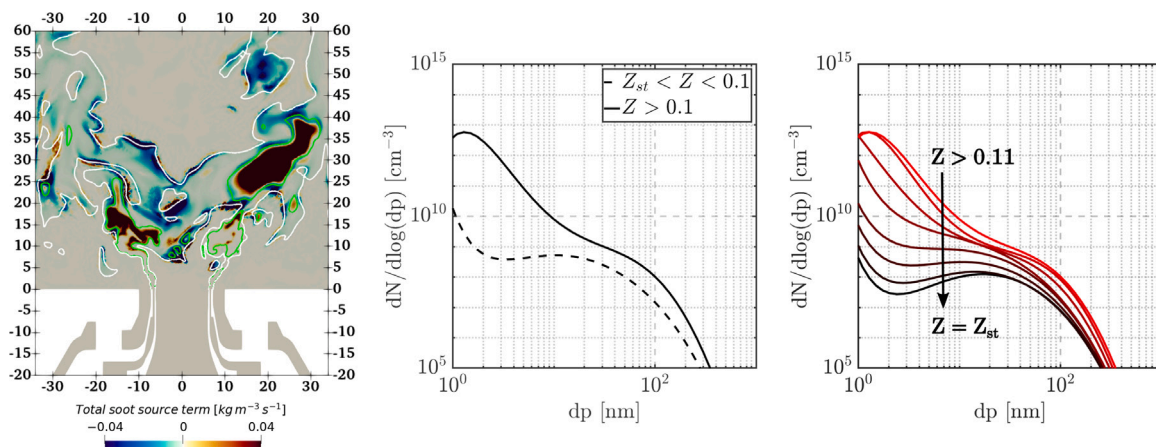


Fig. 15. Spatial-averaged PSD results (Op1). Left: contour of total soot source term in a vertical cut plane. Green line: $Z = 0.1$ isoline, white line: $Z = Z_{st}$ isoline. Center: PSDF in two regions depending on Z . Right: evolution of the PSDF from very rich conditions to Z_{st} . (For interpretation of the references to color in this figure legend, the reader is referred to the web version of this article.)

In order to have a better understanding of the PSD transition when approaching to the stoichiometric region, the plot on the right side presents the spatially averaged PSDF including points conditioned to a more bounded \bar{Z} values, from $\bar{Z} > 0.1$ to $\bar{Z} = Z_{st}$ (red to black). Thus,

when the local mixture level moves from the richer soot formation region to lean conditions, the number of particles slowly decreases and the PSD shape transitions to a more bi-modal like distribution. Due to the strong oxidation along the Z_{st} iso-surface, soot is completely

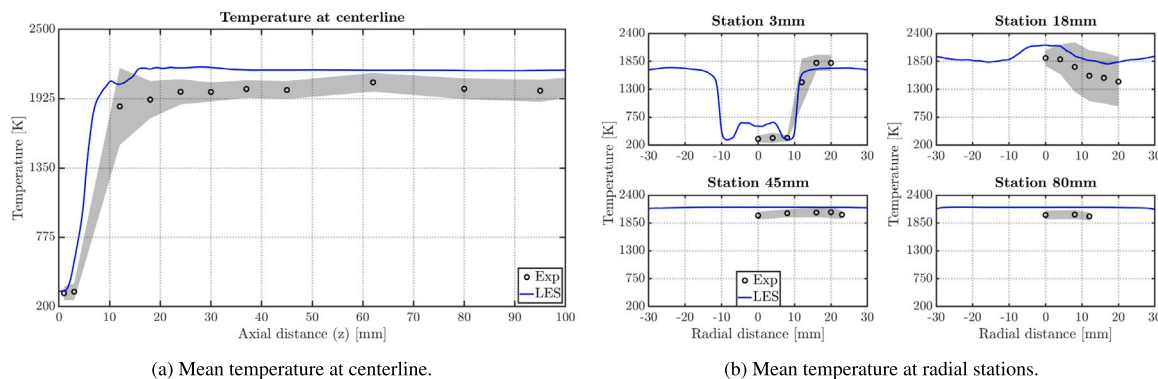


Fig. 16. Comparison between LES results and experiments (Op 2) of temperature. Shaded area: standard deviation of measured temperature.

consumed in the lean regions (e.g. the IRZ in this configuration) and the PSDF is not relevant there.

4.3. Impact of the secondary oxidation air

The results of the DLR pressurized burner without secondary oxidation air (for reference, Op2 in Table 1) are shown in this subsection in order to evaluate its effect on combustion and soot formation and growth. A summary of the gas-phase assessment is presented and soot field predictions and particle size distributions are discussed and compared to Op1.

First, the temperature field comparison between LES results and experimental data at centerline and several stations is illustrated in Fig. 16. In this configuration, the cold air from the secondary injection is not included; thus, temperature increases at the closest axial locations due to the primary reactive region and remains uniform further downstream. The results show the overall trend in axial and radial directions is well captured. However, the accuracy of the predictions is lower compared to the case with secondary air (see Fig. 6a), it shows an overestimation of the temperature along the centerline. Radial profiles also evidence this temperature overprediction downstream in the IRZ. Nevertheless, the temperature values are within the experimental uncertainty on the reacting layers and the model predicts the same temperature distribution across the chamber.

Soot Volume Fraction field is compared with the experimental measurements in Fig. 17 and Fig. 18 presents a comparison at three different axial stations. In general, a good qualitative agreement is achieved and soot distribution inside the combustor is well captured. In this case, the main soot formation phenomena take place at the rich branches following the swirled flow pattern closer to the combustion chamber entry, in a similar way to Op1. A different soot field is observed downstream due to the absence of secondary air jets, which inhibits the oxidation process. In this case, soot generated in the main branches is transported and diluted inside the IRZ, therefore, an almost constant SVF level is observed in this region and further downstream positions. To illustrate this phenomenon, Fig. 19 shows the nucleation, condensation and surface growth source terms for this case. As observed, the main soot production zone is quite similar regardless the secondary oxidation air (note that the scale for soot source terms is the same as in Fig. 13). The main difference can be observed in the nucleation process, which faintly extends over the whole combustion chamber. In spite of that, soot production is still governed by transport due to the flow structures created by the swirling inlet stream pattern in the burner.

As plotted in Fig. 18, the order of magnitude of SVF and radial profiles are correctly predicted and the agreement with the experimental data is satisfactory. Nevertheless, an underestimation of the SVF peak value (~ 50 ppb in LES, ~ 100 ppb in experiments) and the overall magnitude is obtained in the first mid part of the burner, as seen at 18 and 45 mm stations. A better agreement is achieved further downstream, where the soot level slightly decreases close to the axis. There are not many previous studies on numerical modeling that include this operating condition, and in those cases notable discrepancies are found in terms of soot quantity prediction. Chong et al. [64] properly predicted the soot formation region in the branches, but almost no soot in the IRZ using two MoM variants. When using a two-equations semi-empirical model, soot was mainly present in the IRZ but SVF was strongly overestimated. On the other hand, Grader et al. [32] obtained good results for this configuration in terms of soot volume fraction peak value using a sectional approach. However, soot quantity in the IRZ was also underpredicted. In this work, despite the slight underestimation mentioned above, the proposed modeling approach is able to reliably capture the SVF in the shear layers and the recirculation zone.

Finally, PSD are also recovered for this configuration. The results are shown in Fig. 20 in a similar way to the previous section. On the left, a vertical cut plane of the burner is illustrated, colored by the total soot source term. The spatially averaged PSD functions are represented in the plot at the right side. For the PSDF averaging, two different regions are considered: the rich primary soot production zone ($Z > 0.1$) and a region located within the IRZ (see left contour). In this configuration, the absence of secondary air jets leads to a different soot level in the IRZ so it is interesting to evaluate the size distribution in this region. The PSDF obtained at the richer region is similar to the previous case in terms of both the number of particles and shape. This confirms the previous statement that the soot production zone is almost unaffected by the secondary air. On the other hand, the IRZ in this case is characterized by neither soot production nor oxidation, only transport and dilution, as confirmed by the near-zero value of the total soot source term in the IRZ. Therefore, the resulting PSDF has a slightly lower number of particles due to the dilution and low oxidation along the main branches, but the shape of the size distribution is almost unchanged inside this zone.

5. Conclusions

In this work, Large-Eddy Simulations of the reacting flow field and soot formation for the DLR pressurized model combustor have been performed using the FGM-CDSM modeling framework. A modeling strategy based on the tabulation of steady and extinguishing diffusion

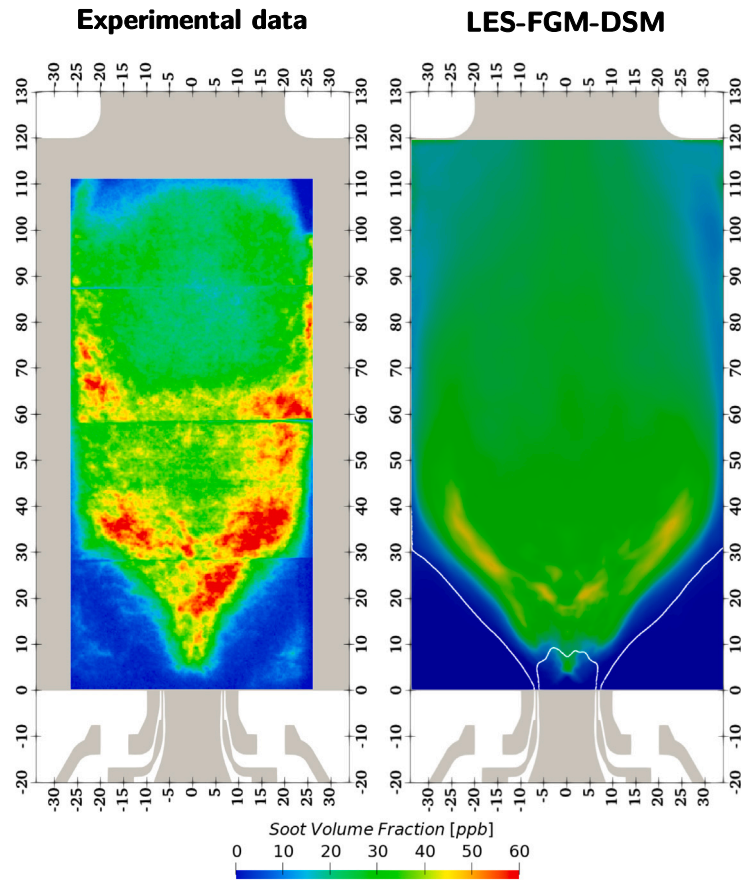


Fig. 17. Comparison of time-averaged Soot Volume Fraction (SVF) contours (Op 2). White line: stoichiometric mixture fraction. Spatial units in mm. (For interpretation of the references to color in this figure legend, the reader is referred to the web version of this article.)

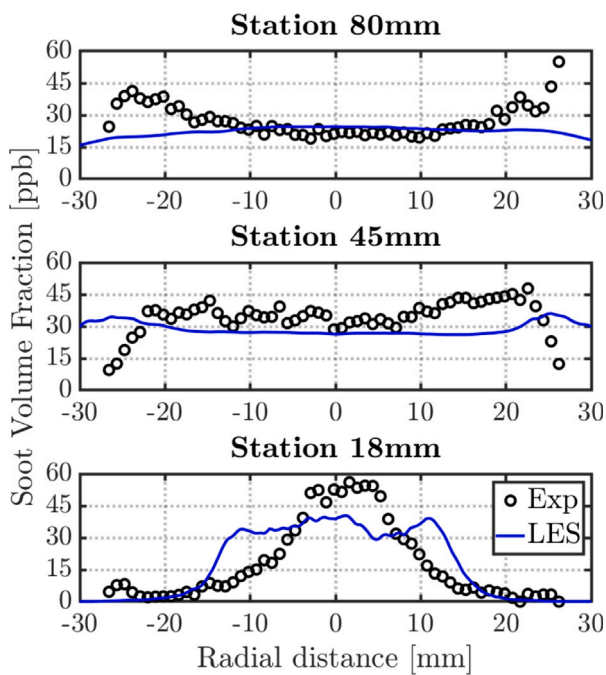


Fig. 18. Comparison between LES results and experiments (Op 2). Soot Volume Fraction (SVF) at different radial stations.

flamelets at different enthalpy levels together with a presumed shape PDF has been employed as turbulent combustion model. Coupled to the combustion model, a discrete sectional method has been evaluated using clustered sections (CDSM) and tabulated soot source terms in the FGM to achieve computationally efficient LES calculations.

The assessment of the gas phase confirms that a good agreement with the experimental diagnostics has been achieved in terms of velocity and temperature fields. Simulations were able to properly capture the swirled flow characteristics, turbulent structures and recirculation regions inside the RQL-like burner.

Soot results have been evaluated and compared with experiments, showing good predictions of soot distribution in the combustion chamber and with a satisfactory agreement on the Soot Volume Fraction magnitude. Regarding the effect of heat losses, relevant discrepancies in results have been found when considering a non-adiabatic approach, obtaining a considerably better agreement in both temperature and SVF fields. Furthermore, LES have been able to reproduce the transient soot processes and dynamics, by reliably capturing the different regions where soot is formed and oxidized. This approach is able to predict that soot persists in the periphery of the combustion chamber, downstream the soot formation region, where other simulations works overestimate oxidation rates.

In addition, Particle Size Distributions have been obtained with the results provided by the sectional soot model. The analysis covers both the temporal evolution of the local PSDF and the spatial-averaged function. In general, an almost uni-modal PSD shape is obtained where the mixture fraction magnitude is high (over ~ 0.1) and, thus, SVF soot

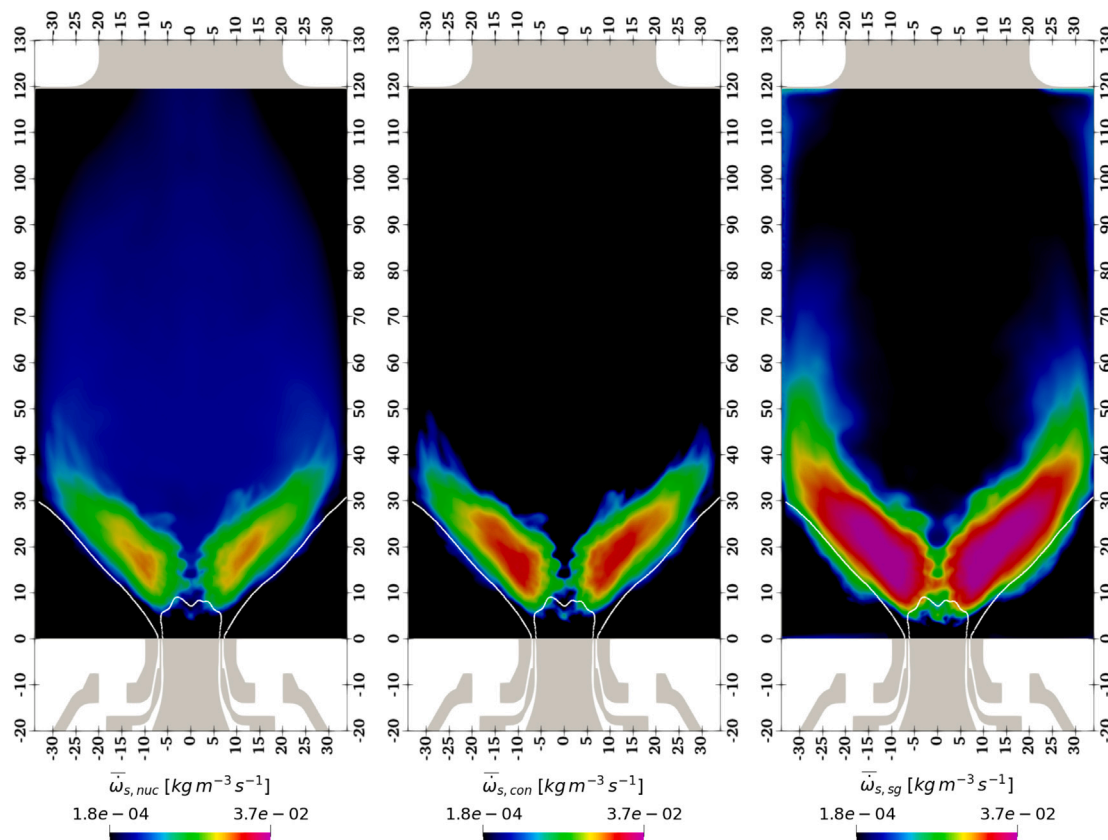


Fig. 19. Time-averaged contours of soot production source terms by subprocess (Op 2). White line: stoichiometric mixture fraction isoline. Legend in log scale. Spatial units in mm. (For interpretation of the references to color in this figure legend, the reader is referred to the web version of this article.)

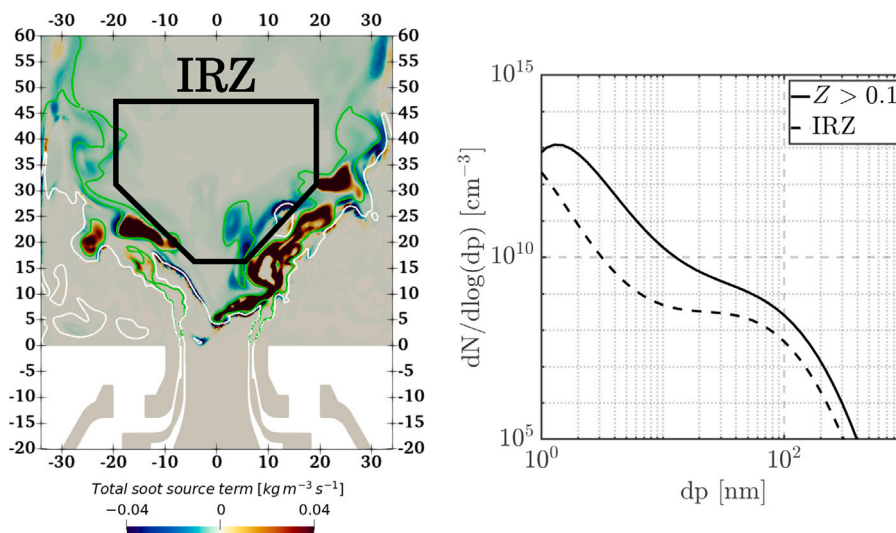


Fig. 20. PSD results for Op2. Left: contour of total soot source term in a vertical cut plane. Green line: $Z = 0.1$ isoline, white line: $Z = Z_{st}$ isoline. Right: spatial averaging of PSDF in two regions: rich region ($Z > 0.1$) and IRZ. (For interpretation of the references to color in this figure legend, the reader is referred to the web version of this article.)

production is important. Furthermore, the model is able to capture the decrease in the number of particles, especially for small sizes, when the local fuel–air ratio approaches to the stoichiometric conditions and the PSDF evolves towards a bi-modal shape. It is interesting to mention that

the clustered sectional approach is able to predict different PSDF shapes according to spatial and temporal variations of soot clusters. Unfortunately, PSD results have not been validated due to the unavailability of their measurement data.

Finally, the effect of excluding the secondary oxidation air has been evaluated by analyzing the corresponding numerical results. In general, a satisfactory agreement was achieved regarding temperature and SVF fields with a slight overprediction of the former and underestimation of the latter. PSD functions were also recovered for this configuration and compared with the previous operating condition. While size distributions are quite similar in the main soot formation region for both cases, the IRZ evidences a slightly different PSDF. Due to the absence of the secondary jets, the central zone of the burner is not affected by soot formation or consumption and the PSDF is slightly modified by soot dilution.

CRedit authorship contribution statement

J.M. García-Oliver: Designed research, Analysed data, Reviewed the paper. **J.M. Pastor:** Performed research, Analysed data, Wrote the paper. **I. Olmeda:** Performed research, Analysed data, Wrote the paper. **A. Kalbhor:** Designed software, Wrote the paper. **D. Mira:** Designed research, Designed software, Reviewed the paper. **J.A. van Oijen:** Designed research, Reviewed the paper.

Declaration of competing interest

The authors declare that they have no known competing financial interests or personal relationships that could have appeared to influence the work reported in this paper.

Acknowledgments

The research leading to these results has received funding from the European Union's Horizon 2020 Programme under the ESTiMatE project, grant agreement No. 821418, and the AHEAD PID2020-118387RB-C33 and SAFLOW TED2021-131618B-C21 and TED2021-131618B-C22 projects from the Ministerio de Ciencia e Innovación, Spain. We acknowledge PRACE for awarding us access through the SootAero project to HAWK at GCS@HLRS, Germany. The authors thankfully acknowledge the computer resources at LaPalma and MareNostrum, and the technical support provided by Instituto de Astrofísica de Canarias (IM-2021-2-0027) and Barcelona Supercomputing Center (IM-2021-3-0016). I. Olmeda acknowledges the Ayuda de Formación de Profesorado Universitario (FPU 18/03065) from the Subprograma de Estatal de Formación del Ministerio de Ciencia, Innovación y Universidades of Spain. DM acknowledges the grant Ayudas para contratos Ramón y Cajal (RYC) 2021: RYC2021-034654-I from Ministerio de Ciencia e Innovación.

Appendix A. Supplementary data

Supplementary material related to this article can be found online at <https://doi.org/10.1016/j.combustflame.2023.113198>.

References

- [1] Daniel Mira, et al., HPC-enabling technologies for high-fidelity combustion simulations, *Proc. Combust. Inst.* (ISSN: 1540-7489) (2022).
- [2] Heinz Pitsch, Large-eddy simulation of turbulent combustion, *Annu. Rev. Fluid Mech.* 38 (2006) 453–482.
- [3] L.Y.M. Gicquel, G. Staffelbach, T. Poinso, Large eddy simulations of gaseous flames in gas turbine combustion chambers, *Prog. Energ. Combust.* 38 (2012) 782–817.
- [4] Stelios Rigopoulos, Modelling of soot aerosol dynamics in turbulent flow, *Flow Turbul. Combust.* 103 (2019) 565–604.
- [5] Venkat Raman, Rodney O. Fox, Modeling of fine-particle formation in turbulent flames, *Annu. Rev. Fluid Mech.* 48 (2016) 159–190.
- [6] Yu Wang, Suk Ho Chung, Soot formation in laminar counterflow flames, *Prog. Energ. Combust.* 74 (2019) 152–238.
- [7] Tarek Echekki, Epaminondas Mastorakos, *Turbulent Combustion Modeling: Advances, New Trends and Perspectives*, Springer Science & Business Media, 2010.
- [8] J.A. Van Oijen, L.P.H. De Goeij, Modelling of premixed laminar flames using flamelet-generated manifolds, *Combust. Sci. Technol.* 161 (2000) 113–137.
- [9] Charles D. Pierce, Parviz Moin, Progress-variable approach for large-eddy simulation of non-premixed turbulent combustion, *J. Fluid Mech.* 504 (2004) 73–97.
- [10] Michael E. Mueller, Heinz Pitsch, LES model for sooting turbulent nonpremixed flames, *Combust. Flame* (6) (2012) 2166–2180.
- [11] Michael E. Mueller, Heinz Pitsch, Large eddy simulation of soot evolution in an aircraft combustor, *Phys. Fluids* 25 (2013) 110812.
- [12] Anne Felden, Eleonore Riber, Benedicte Cuenot, Impact of direct integration of Analytically Reduced Chemistry in LES of a sooting swirled non-premixed combustor, *Combust. Flame* 191 (2018) 270–286.
- [13] Christian Eberle, et al., Toward finite-rate chemistry large-eddy simulations of sooting swirl flames, *Combust. Sci. Technol.* 190 (2018) 1194–1217.
- [14] Martin Grader, Christian Eberle, Peter Gerlinger, Large-Eddy Simulation and analysis of a sooting lifted turbulent jet flame, *Combust. Flame* 215 (2020) 458–470.
- [15] Savvas Gkantonas, et al., Comprehensive soot particle size distribution modelling of a model Rich-Quench-Lean burner, *Fuel* 270 (2020) 117483.
- [16] Michael Frenklach, Method of moments with interpolative closure, *Chem. Eng. Sci.* 57 (2002) 2229–2239, Population balance modelling of particulate systems.
- [17] Fred Gelbard, Yoram Tambour, John H. Seinfeld, Sectional representations for simulating aerosol dynamics, *J. Colloid Interf. Sci.* 76 (1980) 541–556.
- [18] B. Franzelli, A. Vié, N. Darabiha, A three-equation model for the prediction of soot emissions in LES of gas turbines, *Proc. Combust. Inst.* (2018).
- [19] Abhijit Kalbhor, Daniel Mira, Jeroen van Oijen, A computationally efficient approach for soot modeling with the discrete sectional method and FGM chemistry, *Combust. Flame* 255 (2023) 112868.
- [20] Abhijit Kalbhor, Daniel Mira, A. van Oijen Jeroen, Computationally efficient integration of a sectional soot model with FGM chemistry, in: 18th International Conference on Numerical Combustion ; Conference date: 08-05-2022 Through 11-05-2022, 2022.
- [21] Hesheng Bao, et al., Investigation of soot formation in n-dodecane spray flames using LES and a discrete sectional method, *Proc. Combust. Inst.* (2022).
- [22] Klaus Peter Geigle, Redjem Hadeif, Wolfgang Meier, Soot formation and flame characterization of an aero-engine model combustor burning ethylene at elevated pressure, *J. Eng. Gas Turb. Power* 136 (2014).
- [23] Klaus Peter Geigle, et al., Investigation of soot formation in pressurized swirl flames by laser measurements of temperature, flame structures and soot concentrations, *Proc. Combust. Inst.* 35 (35) (2015) 3373–3380.
- [24] International Sooting Flame workshop. URL: <https://www.adelaide.edu.au/cet/isfworkshop/>.
- [25] B. Franzelli, et al., Numerical modeling of soot production in aero-engine combustors using large eddy simulations, in: *Proceedings of the ASME Turbo Expo*, 2015.
- [26] Achim Wick, Frederic Priesack, Heinz Pitsch, Large-eddy simulation and detailed modeling of soot evolution in a model aero engine combustor, in: *Turbo Expo: Power for Land, Sea, and Air*, 2017.
- [27] M.E. Mueller, G. Blanquart, H. Pitsch, Hybrid Method of Moments for modeling soot formation and growth, *Combust. Flame* 156 (2009) 1143–1155.
- [28] Shao Teng Chong, et al., Large eddy simulation of pressure and dilution-jet effects on soot formation in a model aircraft swirl combustor, *Combust. Flame* 192 (2018) 452–472.
- [29] Ömer Hakkı Çokuslu, et al., Soot prediction in a Model Aero-Engine Combustor using a Quadrature-based method of moments, in: *AIAA SciTech Forum*, 2022.
- [30] Steffen Salenbauch, et al., A numerically robust method of moments with number density function reconstruction and its application to soot formation, growth and oxidation, *J. Aerosol. Sci.* 128 (2019) 34–49.
- [31] Pedro Rodrigues, *Modélisation Multiphysique De Flamme Turbulente Suintées Avec La Prise En Compte Des Transferts Radiatifs Et Des Transferts De Chaleur Pariétaux* (Ph.D. thesis), Université Paris-Saclay (ComUE), 2018.
- [32] Martin Grader, et al., LES of a pressurized, sooting aero-engine model combustor at different equivalence ratios with a sectional approach for PAHs and soot, in: *Turbo Expo: Power for Land, Sea, and Air*, 2018.
- [33] N. Peters, Laminar diffusion flamelet models in non-premixed turbulent combustion, *Prog. Energ. Combust.* 10 (1984) 319–339.
- [34] S. Delhay, et al., Incorporating unsteady flow-effects beyond the extinction limit in flamelet-generated manifolds, *Proc. Combust. Inst.* 32 (2009) 1051–1058.
- [35] CHEM1D, A One Dimensional Flame Code, Eindhoven University of Technology.
- [36] Trupti Kathrotia, et al., Combustion kinetics of alternative jet fuels, Part-II: Reaction model for fuel surrogate, *Fuel* 302 (2021) 120736.
- [37] Astrid Ramirez-Hernandez, et al., Reaction model development of selected aromatics as relevant molecules of a kerosene surrogate-the importance of m-xylene within the combustion of 1,3,5-trimethylbenzene, *J. Eng. Gas Turb. Power* 144 (2021).
- [38] Abhijit Kalbhor, Jeroen van Oijen, An assessment of the sectional soot model and FGM tabulated chemistry coupling in laminar flame simulations, *Combust. Flame* 229 (2021) 111381.
- [39] Thierry Poinso, Denis Veynante, *Theoretical and Numerical Combustion*, RT Edwards, Inc, 2005.

- [40] P. Domingo, L. Vervisch, D. Veynante, Large-eddy simulation of a lifted methane jet flame in a vitiated coflow, *Combust. Flame* 152 (2008) 415–432.
- [41] A.W. Vreman, An eddy-viscosity subgrid-scale model for turbulent shear flow: Algebraic theory and applications, *Phys. Fluids* 16 (2004) 3670–3681.
- [42] Ambrus Both, et al., Low-dissipation finite element strategy for low mach number reacting flows, *Comput. & Fluids* 200 (2020) 104436.
- [43] Daniel Mira, et al., Numerical characterization of a premixed hydrogen flame under conditions close to flashback, *Flow Turbul. Combust.* 104 (2020) 479–507.
- [44] Jesus Benajes, et al., Analysis of local extinction of a n-heptane spray flame using large-eddy simulation with tabulated chemistry, *Combust. Flame* 235 (2022) 111730.
- [45] Matthias Ihme, Heinz Pitsch, Prediction of extinction and reignition in nonpremixed turbulent flames using a flamelet/progress variable model. 2. Application in LES of Sandia flames D and E, *Combust. Flame* 155 (2008) 90–107.
- [46] Heinz Pitsch, Chong M. Cha, Sergei Fedotov, Flamelet modelling of non-premixed turbulent combustion with local extinction and re-ignition, *Combust. Theor. Model.* 7 (2003) 317–332.
- [47] Karl Netzell, Harry Lehtiniemi, Fabian Mauss, Calculating the soot particle size distribution function in turbulent diffusion flames using a sectional method, *Proc. Combust. Inst.* 31 (2007) 667–674.
- [48] S.K. Friedlander, *Smoke, Dust and Haze: Fundamentals of Aerosol Dynamics*, Oxford University Press, New York, USA, 2000.
- [49] Michael Frenklach, On surface growth mechanism of soot particles, *Symp. (Int.) Combust.* 26 (1996) 2285–2293.
- [50] Jörg Appel, Henning Bockhorn, Michael Frenklach, Kinetic modeling of soot formation with detailed chemistry and physics: laminar premixed flames of C2 hydrocarbons, *Combust. Flame* 121 (2000) 122–136.
- [51] Cristian A. Hoerlle, Fernando M. Pereira, Effects of CO2 addition on soot formation of ethylene non-premixed flames under oxygen enriched atmospheres, *Combust. Flame* 203 (2019) 407–423.
- [52] Sanjeev Kumar, D. Ramkrishna, On the solution of population balance equations by discretization—I. a fixed pivot technique, *Chem. Eng. Sci.* 51 (1996) 1311–1332.
- [53] Abhijit Kalbhor, Jeroen van Oijen, Effects of hydrogen enrichment and water vapour dilution on soot formation in laminar ethylene counterflow flames, *Int. J. Hydrogen. Energ.* 45 (2020) 23653–23673.
- [54] P. Rodrigues, et al., Coupling an LES approach and a soot sectional model for the study of sooting turbulent non-premixed flames, *Combust. Flame* 190 (2018) 477–499.
- [55] M. Vazquez, et al., Multiphysics engineering simulation toward exascale, *J. Comput. Sci.* 14 (2016) 15–27.
- [56] Klaus Peter Geigle, et al., Flow field characterization of pressurized sooting swirl flames and relation to soot distributions, *Proc. Combust. Inst.* 36 (2017) 3917–3924.
- [57] S.B. Pope, Ten questions concerning the large-eddy simulation of turbulent flows, *New J. Phys. (ISSN: 13672630)* 6 (2004).
- [58] Patrick Nau, et al., Wall temperature measurements at elevated pressures and high temperatures in sooting flames in a gas turbine model combustor, *Appl. Phys. B Lasers Opt.* 123 (2017) 1–8.
- [59] R.S. Mehta, Daniel Connell Haworth, M.F. Modest, Composition PDF/photon Monte Carlo modeling of moderately sooting turbulent jet flames, *Combust. Flame* 157 (2010) 982–994.
- [60] Manedhar Reddy, Ashoke De, Rakesh Yadav, Effect of precursors and radiation on soot formation in turbulent diffusion flame, *Fuel* 148 (2015) 58–72.
- [61] M. Stöhr, et al., Time-resolved study of transient soot formation in an aero-engine model combustor at elevated pressure, *Proc. Combust. Inst.* 37 (2019) 5421–5428.
- [62] Ivan Litvinov, et al., Time-resolved study of mixing and reaction in an aero-engine model combustor at increased pressure, *Combust. Flame* 231 (2021) 111474.
- [63] Livia Tardelli, et al., Impact of the reaction mechanism model on soot growth and oxidation in laminar and turbulent flames, in: *Turbo Expo: Power for Land, Sea, and Air*, 2019.
- [64] Shao Teng Chong, et al., Effect of soot model, moment method, and chemical kinetics on soot formation in a model aircraft combustor, *Proc. Combust. Inst.* 37 (2019) 1065–1074.